Supporting Information:
Separation of Specific Single Enantiomer Single-Wall Carbon Nanotubes in the Large Diameter Regime

Han Li,[†*] Georgy Gordeev,[#] Oisin Garrity,[#] Naga Anirudh Peyyety,[†‡] Pranauv Balaji Selvasundaram,[†‡] Simone Dehm,[†] Ralph Krupke,[†‡] Sofie Cambré,[¶] Wim Wenseleers,[¶] Stephanie Reich,[#] Ming Zheng,[§] Jeffrey A. Fagan[§*] and Benjamin S. Flavel[†*]

† Institute of Nanotechnology, Karlsruhe Institute of Technology, Karlsruhe, 76021 Germany.

Department of Physics, Freie Universität Berlin, Berlin 14195, Germany.

‡ Institute of Materials Science, Technische Universität Darmstadt, Darmstadt 64287 Germany.

¶ Physics Department, University of Antwerp, Antwerp 2020, Belgium.

§ Materials Science and Engineering Division, National Institute of Standards and Technology, Gaithersburg MD 20899, USA.

* han.li@kit.edu, jeffrey.fagan@nist.gov & benjamin.flavel@kit.edu

ORCID:
Han Li: 0000-0002-0597-8409
Georgy Gordeev: 0000-0002-3273-2105
Ralph Krupke: 0000-0001-8427-8592
Sofie Cambré: 0000-0001-7471-7678
Wim Wenseleers: 0000-0002-3509-0945
Stephanie Reich: 0000-0002-2391-0256
Ming Zheng: 0000-0002-8058-1348
Jeffrey A. Fagan: 0000-0003-1483-5554
Benjamin S. Flavel: 0000-0002-8213-8673

Certain equipment, instruments or materials are identified in this paper in order to adequately specify the experimental details. Such identification does not imply recommendation by the National Institute of Standards and Technology (NIST) nor does it imply the materials are necessarily the best available for the purpose.

Table of Contents

Acronyms

Analytical Ultracentrifugation (AUC)

Aqueous Two-Phase Extraction (ATPE)

Circular Dichroism (CD)

Density Gradient Ultracentrifugation (DGU)

Dextran (DX)

Electric Arc-Discharge (EA)

Field Effect Transistor (FET)

Laser Vaporization (LV)

Photoluminescence Excitation (PLE)

Plasma Torch (PT)

Polyethylene Glycol (PEG)

Resonant Raman Scattering (RRS)

Radial Breathing Mode (RBM)

Single-Wall Carbon Nanotubes (SWCNTs)

Sodium Cholate (SC)

Sodium Deoxycholate (DOC)

Sodium Dodecyl Sulphate (SDS)

D_t = Nanotube Diameter

$S_{11,\ 22,\ 33,\ 44}$ = Semiconducting Carbon Nanotube Optical Transitions

$M_{11,\ 22}$ = Metallic Carbon Nanotube Optical Transitions

$T_{1,2,3,\ldots n}$ = Top Phase Fractions

$B_{1,2,3,\ldots n}$ = Bottom Phase Fractions

PLE Fitting to Determine Purity

The empirical fitting model used to fit the PLE maps is based on the previous two-dimensional fitting procedure described previously in the supporting information of reference.[1] The empirical model is based on a 2D function describing the PLE spectrum of each individual chirality, and a linear combination of these 2D basis functions to make up the full PLE map of a given sample.

The 2D fit function for each chirality is built up out of an emission and excitation line shape:

(i) The emission line shape is modeled using a Voigt line shape centered at the transition energy S_{11}. In addition a phonon side band corresponding to the Radial Breathing Mode vibrational frequency is added at the low energy side of the S_{11} peak. The position of this phonon position is not fitted, but instead determined *via* the empirical formula derived by Bachilo *et al.*[2] for the Raman shift: $\omega_{RBM} = \frac{223.5}{d} + 12.5$ where d is the diameter (in nm) of the nanotube. Determination of this diameter is done by inverting the empirical relations for the electronic transitions derived by Bachilo *et al*.[2] and later adapted for empty SWCNTs in ref,[3] providing S_{11} and S_{22} with respect to diameter and chiral angle. In order to reduce the number of fit parameters, the line shape of this phonon side band is taken exactly the same as the S_{11} peak, with identical line width, so that only the relative amplitude of this phonon side band with respect to the S_{11} peak is a fit parameter. To account for the differences in electron-phonon coupling for different SWCNTs, a diameter-dependent amplitude of this phonon side band, A_{RBM}, was included in the fit, in the form of $A_{\mathrm{RBM}} = A.d^{-\alpha}$, with A and α fitting parameters. (For those PLE maps where only one or a few chiralities are present, the parameter α was fixed and only A was fitted.)

(ii) The excitation line shape is modeled taking into account both excitonic and band-to-band absorptions:

1. The S_{22} excitonic transition is also modeled using a Voigt line shape centered at the transition energy S_{22}.
2. Band-to-band transitions are modeled as $\propto 1/\sqrt{S - S_{22}}$ convoluted with a Gaussian profile with the same full width at half maximum as that of the excitonic Voigt line shape, to avoid this function to become infinite at $S=S_{22}$. Similarly, also a band-to-band absorption associated with the first optical

transition S_{11} is included, only the high energy tail of which is used to account for absorption at longer wavelengths than the S_{22} excitonic absorption. The amplitude of the band-to-band absorption contribution is fitted as a relative value with respect to the amplitude of the corresponding S_{22} excitonic transition, and is taken the same for all chiralities.

3. A phonon side-band, residing at approx. 0.2 eV above the S_{22} excitation is also included in the excitation profile. Its precise position is fitted, but for simplicity is common for all the SWCNT chiralities, and its line shape and width are taken the same as the line width for the excitonic S_{22} contribution. To account for the differences in electron-phonon coupling for different SWCNTs, a diameter-dependent amplitude of this phonon side band, A_{ph}, was included in the fit, in the form of $A_{ph} = A.d^{-\alpha}$, with A and α fitting parameters. The amplitude A, is again fitted as a relative value with respect to the amplitude of the corresponding S_{22} excitonic transition, and is taken the same for all chiralities. Note that A and α are different values than those of the RBM phonon side band described above.

(iii) Finally, the so-obtained emission and excitation profiles are combined into a 2D fitting function for each chiral structure – of which the S_{22} excitonic transition amplitudes are determined by a simple (analytical) linear regression. As such these amplitudes do not require numerical optimization.

The different PLE maps, of samples originating from the same semi-parent suspension were fitted simultaneously, i.e. the fit parameters (i.e. peak positions and line widths, as described in sections (i) and (ii)) of the above-mentioned model were optimized simultaneously for the different samples (shared values), while the relative amplitudes of the band-to-band transitions and phonon side bands with respect to the S_{11} and S_{22} exciton were optimized individually for each sample. By doing so, the intensities of all chiral species present in the parent samples can be extracted in a more reliable manner also for the other samples, even when a chirality is absent (zero amplitude). To avoid negative amplitudes compensating for imperfect fitting of other chiralities, during the linear regression of the amplitudes a condition is implemented that all amplitudes must be positive.

Tabulated Conditions for (n,m) Structure Separations

Stage 1				Stage 2			
Fraction	Bottom Phase (Dextran) volume (mL)	Top Phase (PEG) volume (mL)	HCl (0.5 mol/L) volume (mL)	Fraction	Bottom Phase (Dextran) volume (mL)	Top Phase (PEG) volume (mL)	HCl (0.5 mol/L) volume (mL)
T_1	5	10	0.26	T_4T_1	5	10	0.15
T_2	5	10	0.16	T_4T_2	5	10	0.20
T_3	5	10	0.22	T_4T_3	5	5	0.15
T_4	5	10	0.22	T_5T_1	5	10	0.24
T_5	5	10	0.22	T_5T_2	5	10	0.20
T_6	5	10	0.18	T_5T_3	5	10	SDS
T_7	5	10	0.24	$T_{7\text{-}8}T_1$	5	10	0.25
T_8	5	10	0.20	$T_{7\text{-}8}T_2$	5	10	0.20
T_9	5	10	0.24	$T_{7\text{-}8}T_3$	5	10	SDS
T_{10}	5	10	0.20				
T_{11}	5	10	0.20				
T_{12}	5	15	0.30				

Supplementary Table S1. Volume of the PEG and DX mimic phases containing surfactants and the amount of HCl added at each stage and step of separation for the $C_{16}H_{34}$@EA semiconducting parent. SDS in the HCl column indicates that a final aliquot of 4.5% SDS was added instead of HCl to ensure that all SWCNTs were partitioned into the PEG phase.

Stage 1				Stage 2			
Fraction	Bottom Phase (Dextran) volume (mL)	Top Phase (PEG) volume (mL)	HCl (0.5 mol/L) volume (mL)	Fraction	Bottom Phase (Dextran) volume (mL)	Top Phase (PEG) volume (mL)	HCl (0.5 mol/L) volume (mL)
T_1	5	10	0.20	T_2T_1	4	8	0.05
T_2	4	8	0.15	T_2T_2	4	2	0.05
T_3	4	8	0.14	T_4T_1	4	8	0.05
T_4	4	8	0.18	T_4T_2	4	4	0.10
T_5	4	8	0.18	T_5T_1	4	8	0.03
T_6	4	8	0.20	T_5T_2	4	4	0.05
T_7	4	8	0.22	T_6T_1	4	8	0.02
T_8	4	8	0.24	T_6T_2	4	4	0.05
T_9	4	8	SDS	T_7T_1	4	8	0.04
T_{10}	4	8	SDS	T_7T_2	4	4	0.05
				T_8T_1	4	8	0.01
				T_8T_2	4	4	0.10
				T_8T_3	4	4	0.20

Supplementary Table S2. Volume of the PEG and DX mimic phases containing surfactants and the amount of HCl added at each stage and step of separation for the $C_{16}H_{34}$@EA metallic parent. SDS in the HCl column indicates that a final aliquot of 4.5% SDS was added instead of HCl to ensure that all SWCNTs were partitioned into the PEG phase.

Stage 1				Stage 2			
Fraction	Bottom Phase (Dextran) volume (mL)	Top Phase (PEG) volume (mL)	HCl (0.5 mol/L) volume (mL)	Fraction	Bottom Phase (Dextran) volume (mL)	Top Phase (PEG) volume (mL)	HCl (0.5 mol/L) volume (mL)
T_1	5	10	0.22	T_3T_1	5	10	0.04
T_2	5	10	0.14	T_3T_2	5	5	0.12
T_3	5	10	0.20	T_4T_1	5	10	0.06
T_4	5	10	0.24	T_4T_2	5	5	0.08
T_5	5	10	0.25	T_4T_3	5	5	0.12
T_6	5	10	0.25	T_4T_4	5	5	0.15

Supplementary Table S3. Volume of the PEG and DX mimic phases containing surfactants and the amount of HCl added at each stage and step of separation for the Empty@EA-AP semiconducting parent. SDS in the HCl column indicates that a final aliquot of 4.5% SDS was added instead of HCl to ensure that all SWCNTs were partitioned into the PEG phase.

Stage 1				Stage 2			
Fraction	Bottom Phase (Dextran) volume (mL)	Top Phase (PEG) volume (mL)	HCl (0.5 mol/L) volume (mL)	Fraction	Bottom Phase (Dextran) volume (mL)	Top Phase (PEG) volume (mL)	HCl (0.5 mol/L) volume (mL)
T_1	4	8	0.15	T_4T_1	3	6	0.06
T_2	4	8	0.14	T_4T_2	3	6	0.15
T_3	3	6	0.10	T_4T_3	3	6	0.20
T_4	3	6	0.15				
T_5	3	6	0.14				
T_6	3	6	0.15				
T_7	3	6	0.18				
T_8	3	6	SDS				
T_9	3	6	SDS				

Supplementary Table S4. Volume of the PEG and DX mimic phases containing surfactants and the amount of HCl added at each stage and step of separation for the Empty@EA-AP metallic parent. SDS in the HCl column indicates that a final aliquot of 4.5% SDS was added instead of HCl to ensure that all SWCNTs were partitioned into the PEG phase.

Stage 1				Stage 2			
Fraction	Bottom Phase (Dextran) volume (mL)	Top Phase (PEG) volume (mL)	HCl (0.5 mol/L) volume (mL)	Fraction	Bottom Phase (Dextran) volume (mL)	Top Phase (PEG) volume (mL)	HCl (0.5 mol/L) volume (mL)
T_1	5	10	0.25	T_3T_1	0.1	1	0.02
T_2	5	10	0.18	T_3T_2	0.1	1	0.02
T_3	5	10	0.20	T_3T_3	0.1	1	0.04
T_4	5	10	0.22				
T_5	5	10	0.23				
T_6	5	10	0.25				

Supplementary Table S5. Volume of the PEG and DX mimic phases containing surfactants and the amount of HCl added at each stage and step of separation for the H_2O@EA semiconducting parent.

Stage 1				Stage 2			
Fraction	Bottom Phase (Dextran) volume (mL)	Top Phase (PEG) volume (mL)	HCl (0.5 mol/L) volume (mL)	Fraction	Bottom Phase (Dextran) volume (mL)	Top Phase (PEG) volume (mL)	HCl (0.5 mol/L) volume (mL)
T_1	0.2	1	0.02	$T_{2\text{-}4}T_1$	2	2	0
T_2	0.25	0.8	0.014	$T_{2\text{-}4}T_2$	2	2	0.02
T_3	0.3	0.8	0.014	$T_{2\text{-}4}T_3$	2	2	0.03
T_4	0.3	0.8	0.015	$T_{2\text{-}4}T_4$	2	2	0.035
T_5	0.3	0.8	0.017	$T_{2\text{-}4}T_5$	2	2	0.035
T_6	0.3	0.8	0.017	$T_{2\text{-}4}T_6$	2	2	0.04
				$T_{2\text{-}4}T_7$	2	2	0.05

Supplementary Table S6. Volume of the PEG and DX mimic phases containing surfactants and the amount of HCl added at each stage and step of separation for the H_2O@EA2 semiconducting parent.

Stage 1				Stage 2			
Fraction	Bottom Phase (Dextran) volume (mL)	Top Phase (PEG) volume (mL)	HCl (0.5 mol/L) volume (mL)	Fraction	Bottom Phase (Dextran) volume (mL)	Top Phase (PEG) volume (mL)	HCl (0.5 mol/L) volume (mL)
T_1	5	5	0.16	T_1T_1	2.5	5	0.01
T_2	5	5	0.12	T_1T_2	2.5	5	0.10
T_3	5	5	0.12	T_2T_1	2.5	5	0.02
T_4	5	5	0.10	T_2T_2	2.5	5	0.07
T_5	5	5	0.12	T_2T_3	2.5	5	0.11
T_6	5	5	0.14	T_2T_4	2.5	5	SDS
				T_3T_1	2.5	5	0.03
				T_3T_2	2.5	5	0.15
				T_6T_1	2.5	5	0.12
				T_6T_2	2.5	2.5	SDS

Supplementary Table S7. Volume of the PEG and DX mimic phases containing surfactants and the amount of HCl added at each stage and step of separation for the $C_{24}H_{50}$@PT semiconducting parent. SDS in the HCl column indicates that a final aliquot of 4.5% SDS was added instead of HCl to ensure that all SWCNTs were partitioned into the PEG phase.

Absorbance Spectra and Photographs Documenting Separations of Different SWCNT Materials

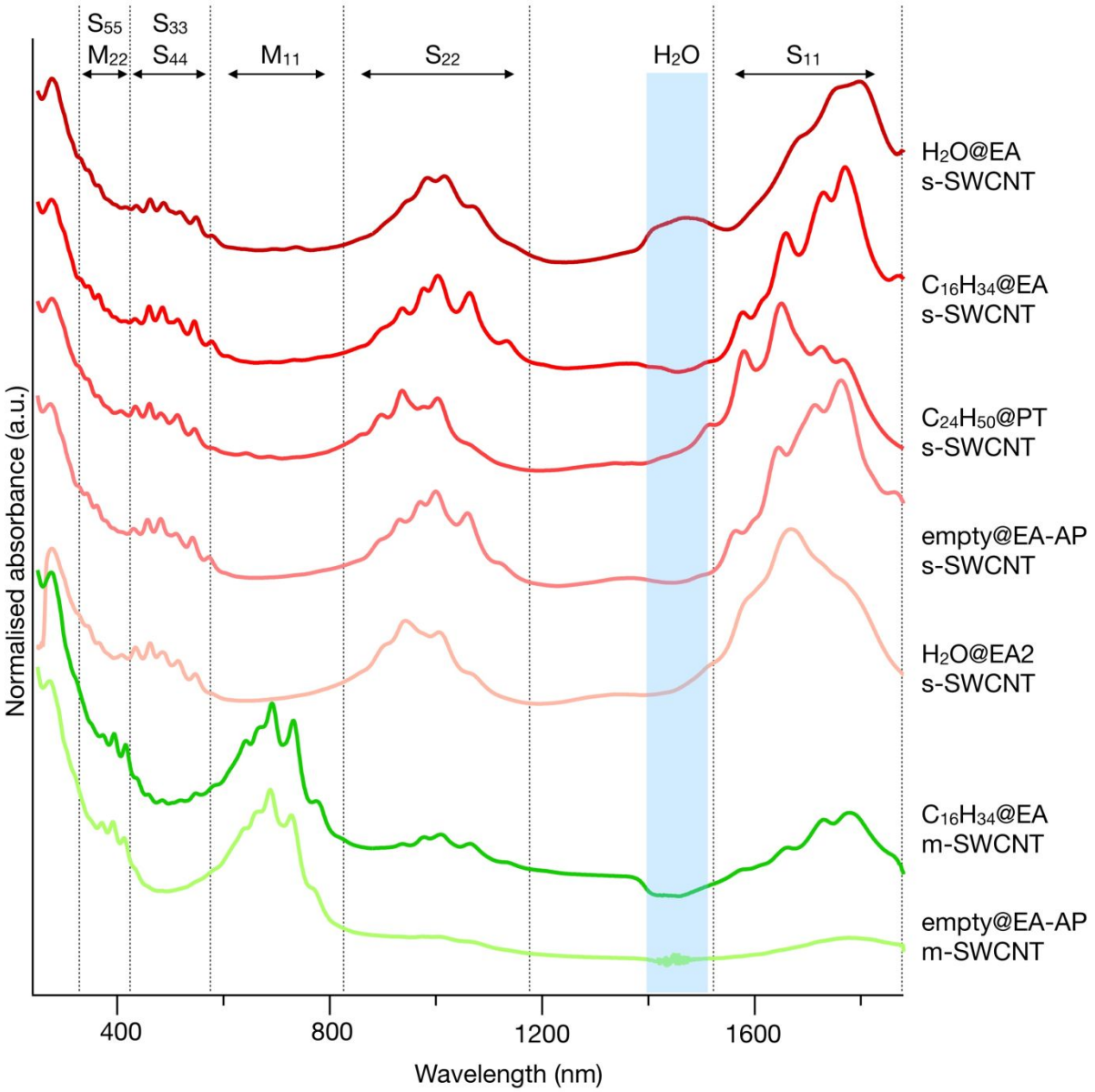

Supplementary Figure S1. Absorption spectra of the semiconducting (*s*-) and metallic (*m*-) SWCNT parent suspensions in H_2O from the various raw materials (EA, PT, EA-AP, EA2) with different endohedral filling ($C_{16}H_{34}$, $C_{24}H_{50}$, H_2O) or empty used in this work. The spectra are normalised at 830 nm and offset vertically for better comparison.

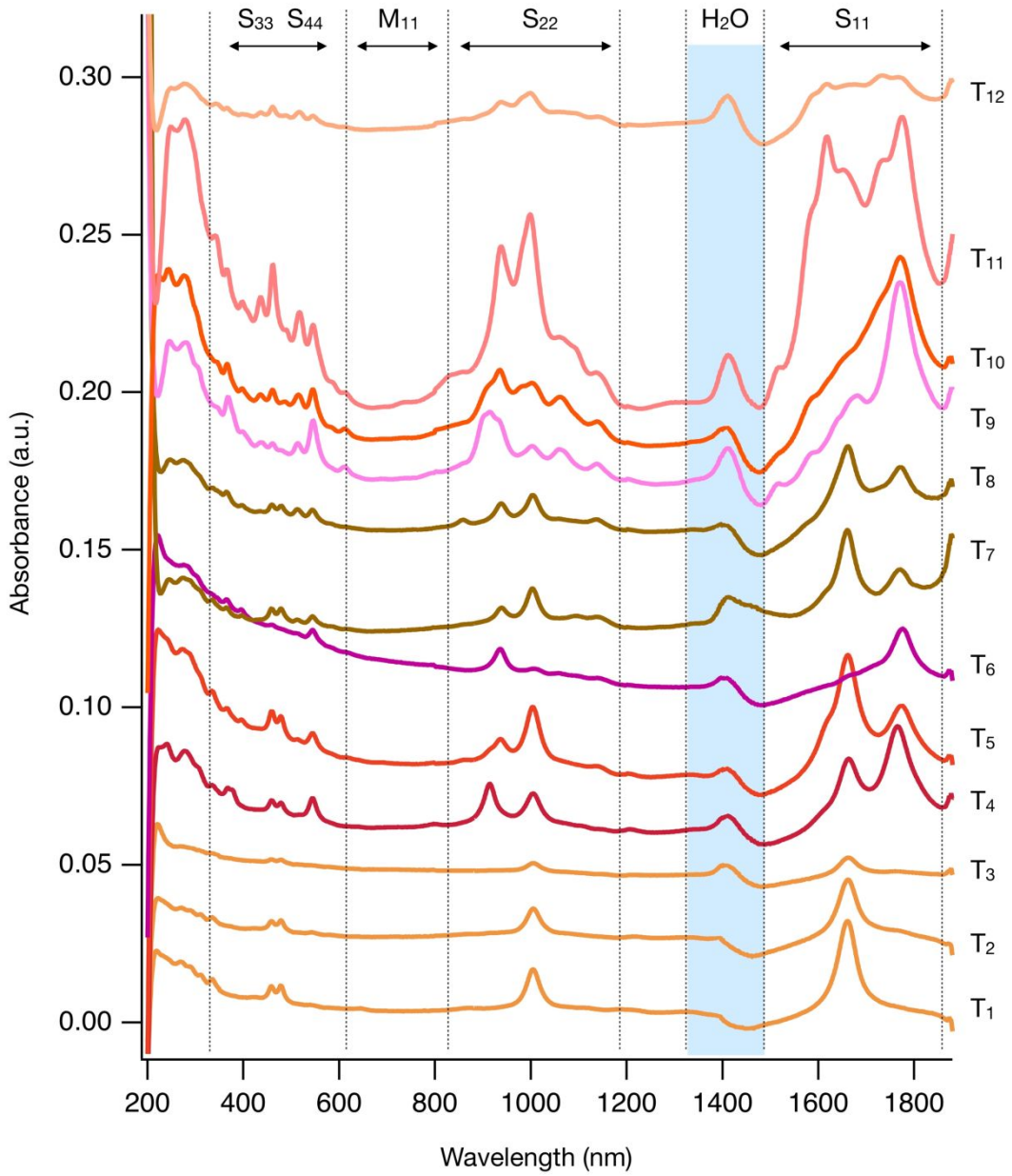

Supplementary Figure S2. All fractions obtained in Stage 1 for the $C_{16}H_{34}$@EA semiconducting parent *via* sequential HCl additions ($T_1 - T_{12}$) in H_2O before ultrafiltration. In all cases the top phase (T_n, PEG) was removed for measurement and replaced by fresh mimic top phase before adding further HCl. $T_1 - T_6$ are identical to the spectra shown in Figure 2 (a).

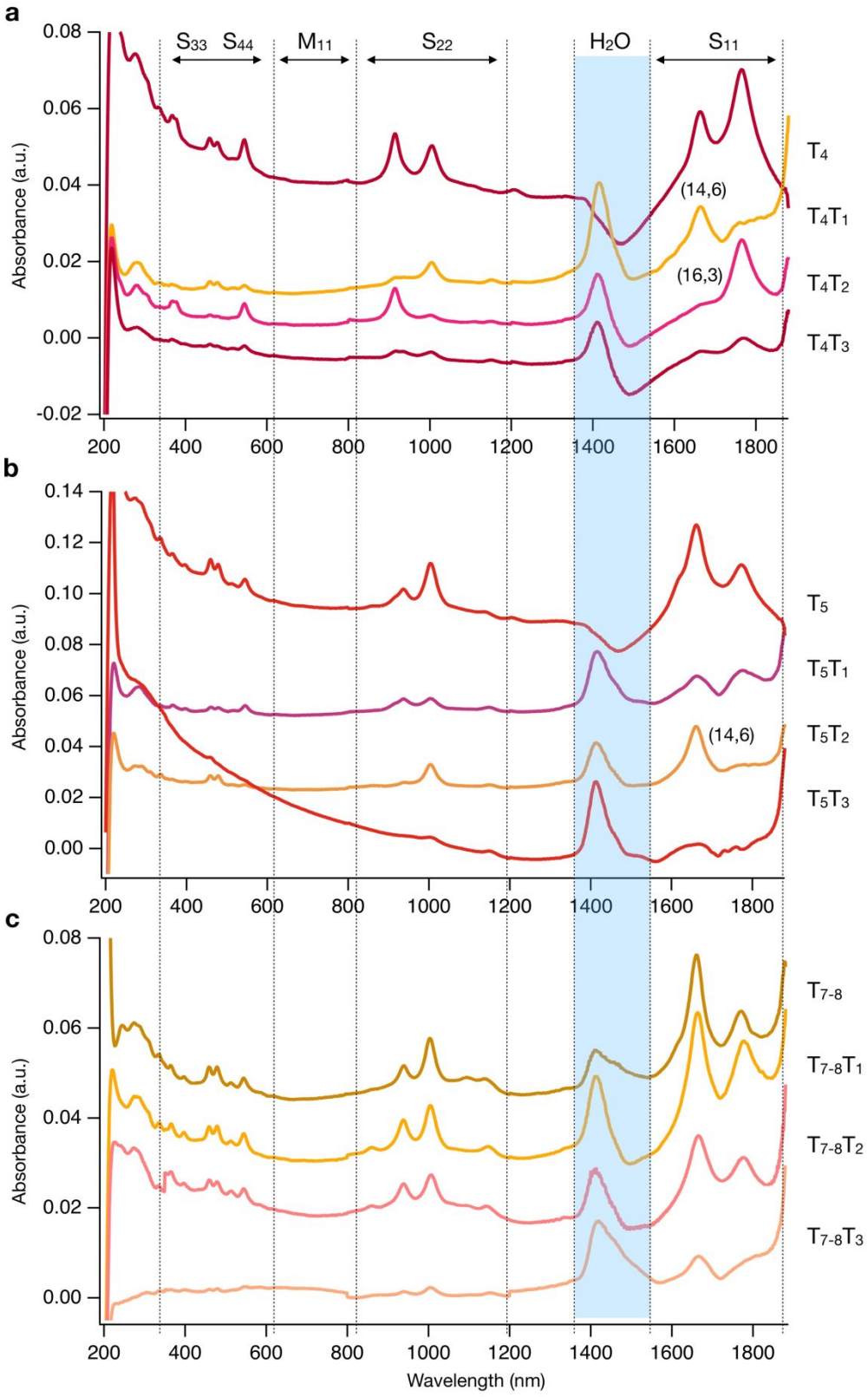

Supplementary Figure S3. Stage 2 enrichment of fractions (a) T_4, (b) T_5 and (c) $T_{7\text{-}8}$ shown in Figure S2 and obtained from the $C_{16}H_{34}$@EA semiconducting parent in H_2O before ultrafiltration. Prior to the sequential addition of HCl, fresh bottom phase (dextran) was added to re-establish the two-phase system and in all cases the top phase (T_nT_m, PEG) was removed for measurement and replaced by fresh mimic top phase before adding further HCl. Fractions T_7 & T_8 (Figure S1) were combined to obtain $T_{7\text{-}8}$.

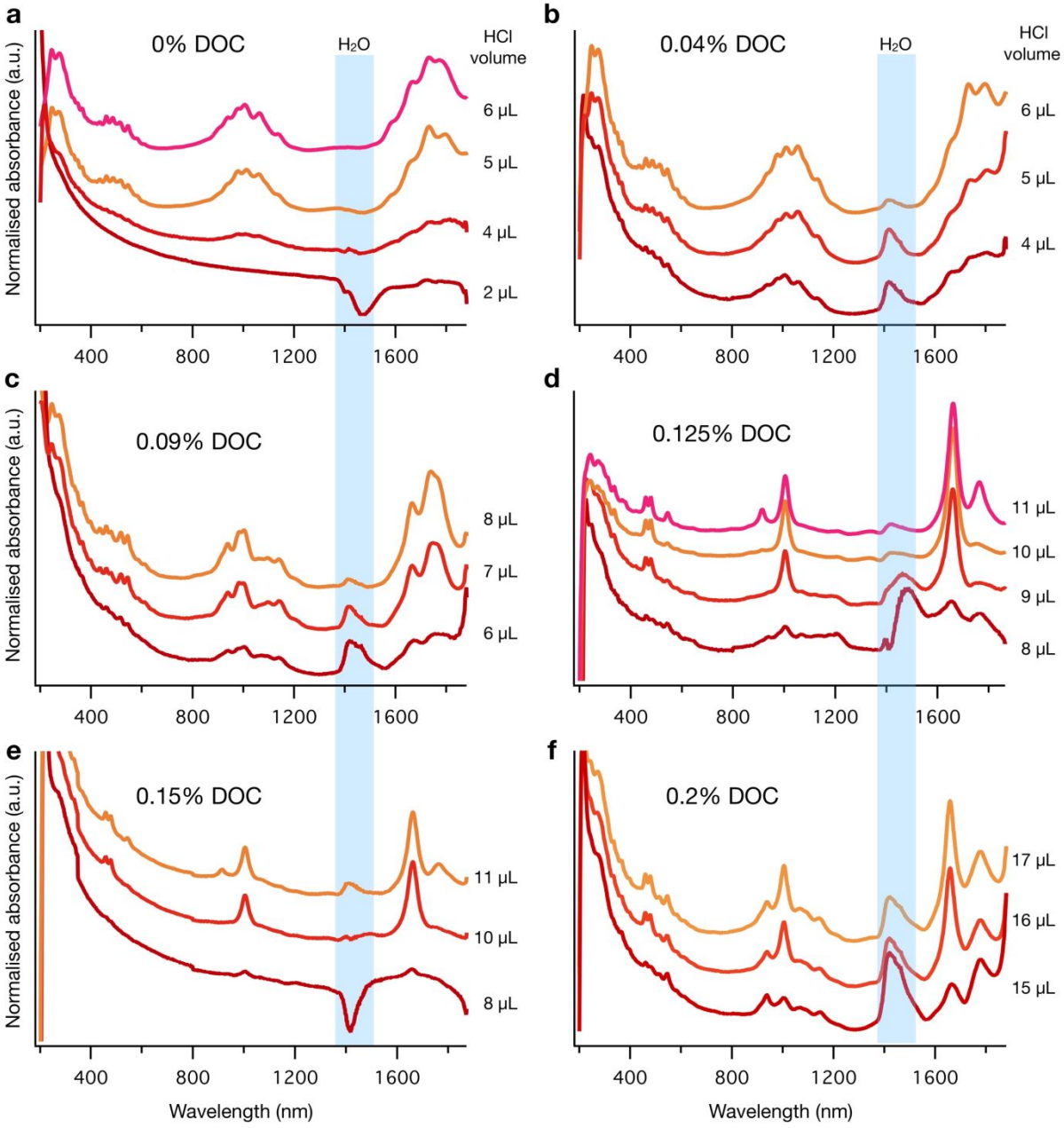

Supplementary Figure S4. Modulation of the DOC concentration in Stage 1 for (14,6) separation with a fixed concentration of 0.225% SDS and 0.9% SC. Indicated volumes of 0.5 mol/L HCl were added to 0.6 mL suspensions (0.1 mL bottom phase, 0.5 mL top phase) from 0% to 0.2% DOC (a - f). All spectra are from top phase and measured in H_2O before ultrafiltration.

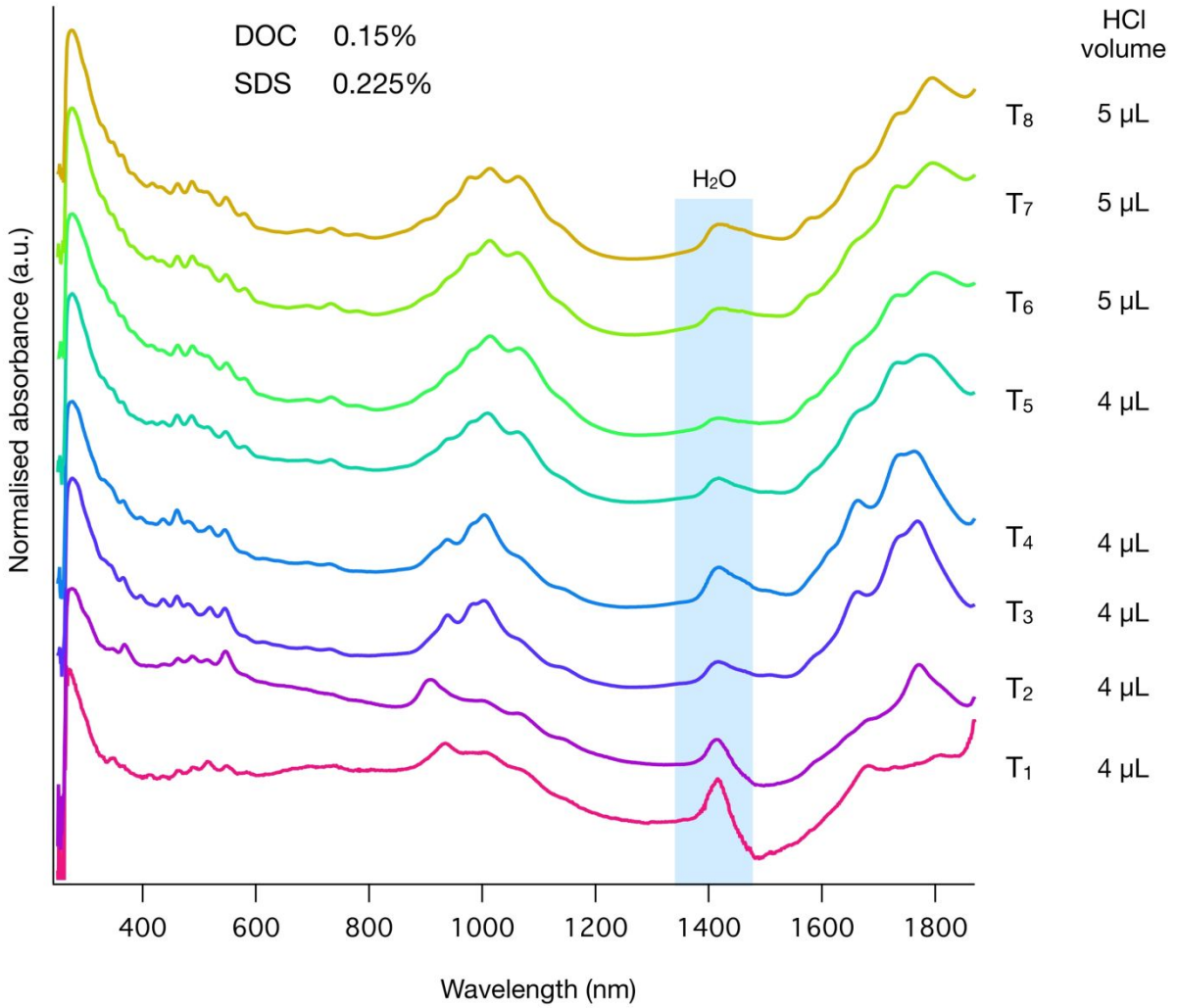

Supplementary Figure S5. Stage 1 fractions of separation with a fixed concentration of 0.15% DOC / 0.225% SDS and no SC were obtained from $C_{16}H_{34}$@EA semiconducting parent. Indicated volumes of 0.5 mol/L HCl were added to 1 mL suspensions (0.2 mL bottom phase, 0.8 mL top phase). All spectra are measured in H_2O before ultrafiltration.

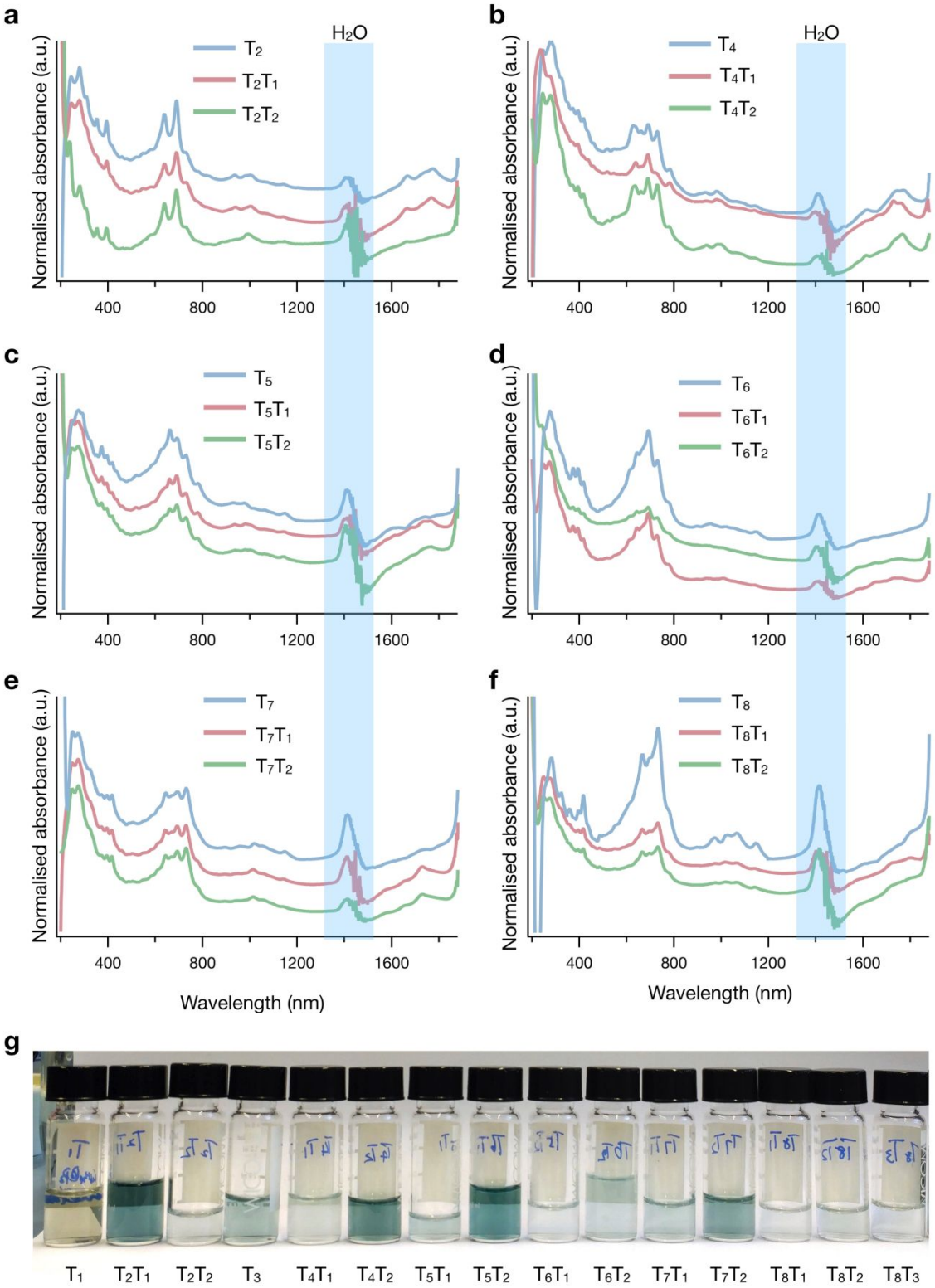

Supplementary Figure S6. Stage 2 enrichment of fractions T_2, $T_4 - T_8$ (a, b, c, d, e, f) shown in Figure 4 (c) obtained from the $C_{16}H_{34}$@EA metallic parent. Prior to the sequential addition of HCl, fresh bottom phase (dextran) was added to re-establish the two-phase system and in all cases the top phase (T_nT_m, PEG) was removed for measurement and replaced by fresh mimic top phase before adding further HCl. (g) a photograph provides the reader with an appreciation of the color and optical density of the resulting fractions. The spectra are normalised at 270 nm and offset vertically for better comparison. All spectra are measured in H_2O.

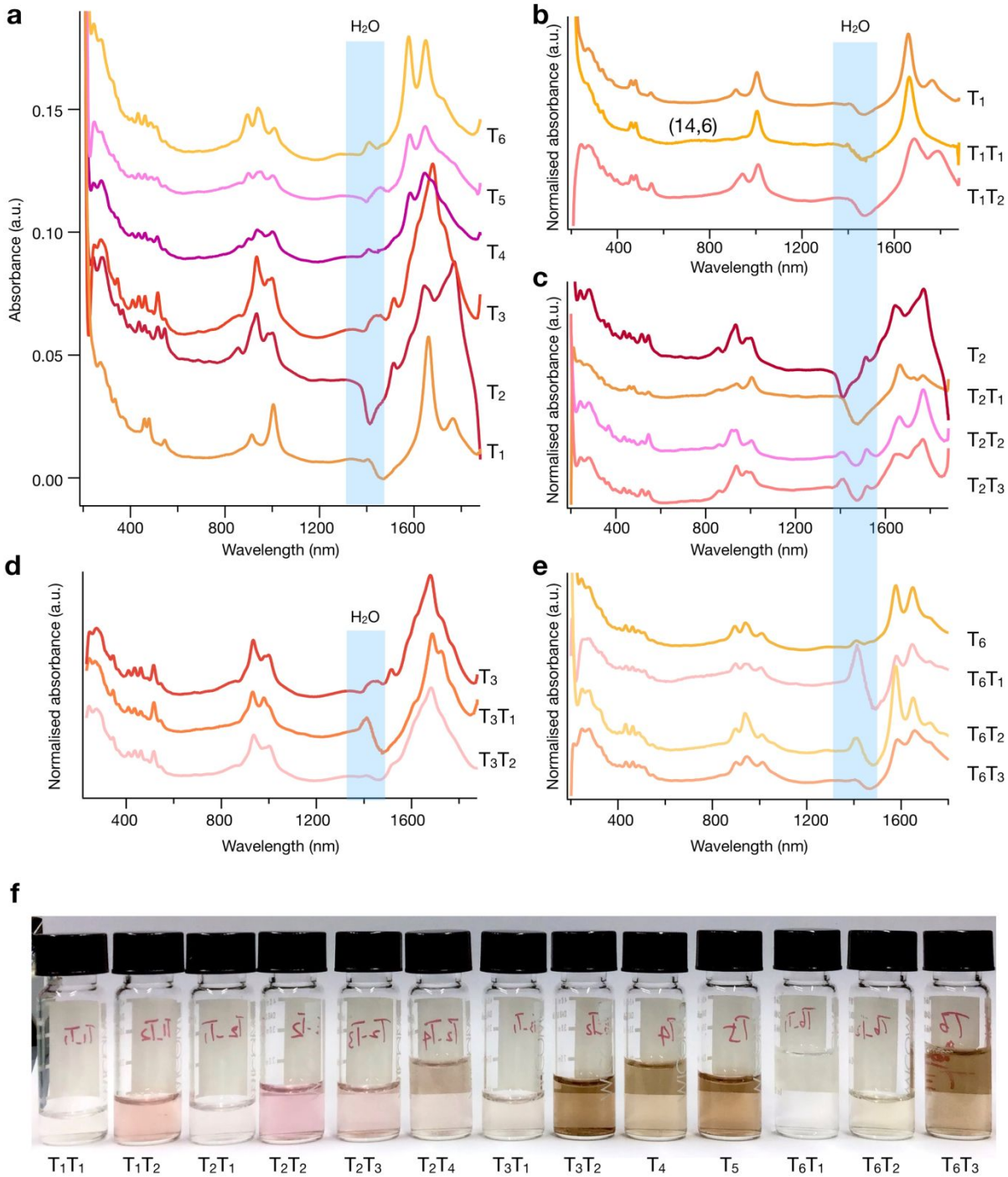

Supplementary Figure S7. Separation of the $C_{24}H_{50}$@PT (Raymor) semiconducting parent to demonstrate the robustness of our approach. (a) absorption spectra of Stage 1 fractions in H_2O (T_1 – T_6). T_1, T_2, T_3, and T_6 are further processed at Stage 2 and their absorption spectra are shown in (b), (c), (d) and (e), respectively. (f) a photograph provides the reader with an appreciation of the color and optical density of the resulting fractions. In all cases the top phase (T_n, PEG) was removed for measurement and replaced by fresh mimic top phase before adding further HCl. The spectra are normalised at 270 nm and offset vertically for better comparison.

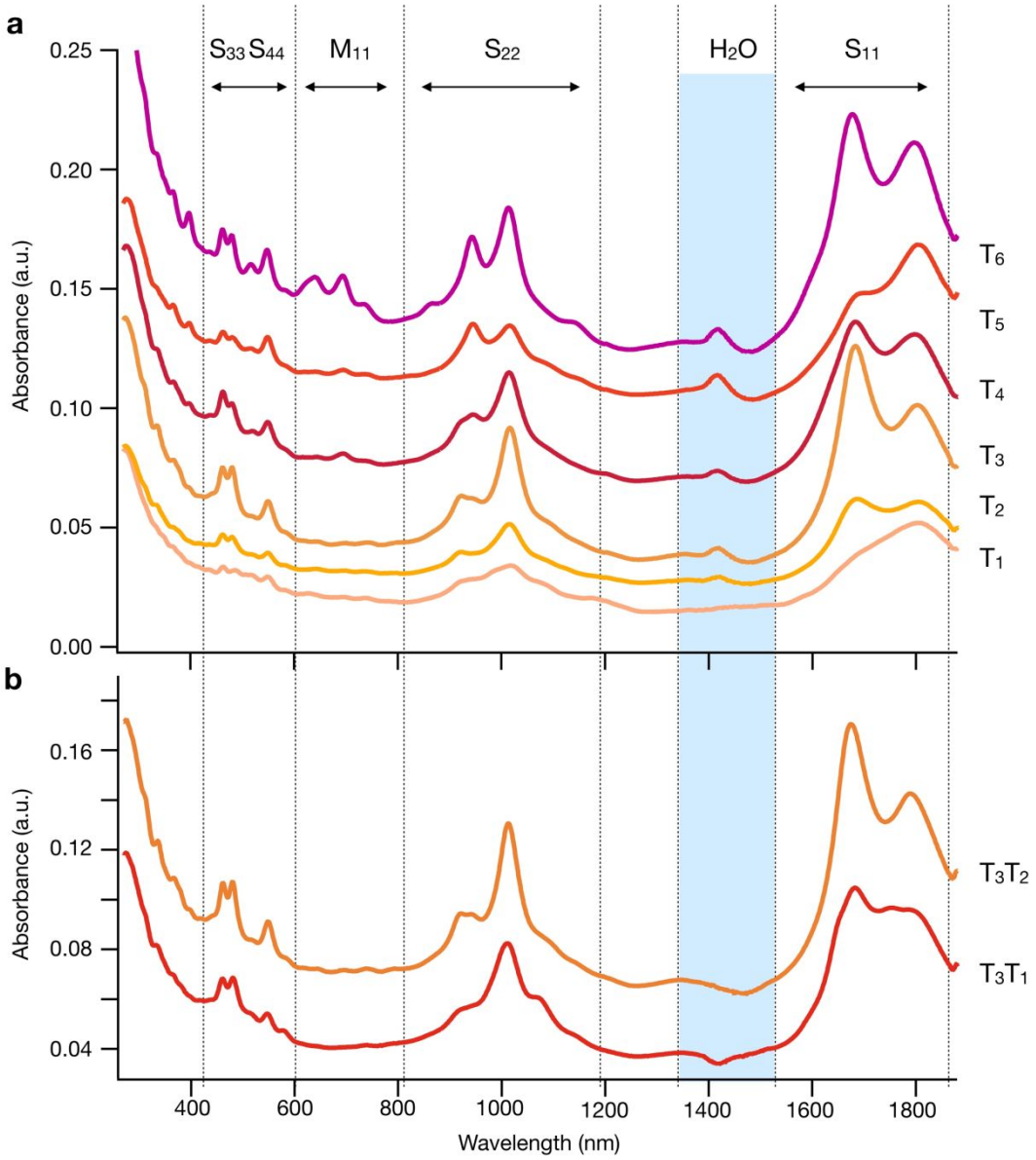

Supplementary Figure S8. Separation of H_2O@EA semiconducting SWCNTs. (a) absorption spectra of Stage 1 fractions in H_2O (T_1 – T_6). T_3 was further processed in Stage 2 and the corresponding spectra are shown in (b).

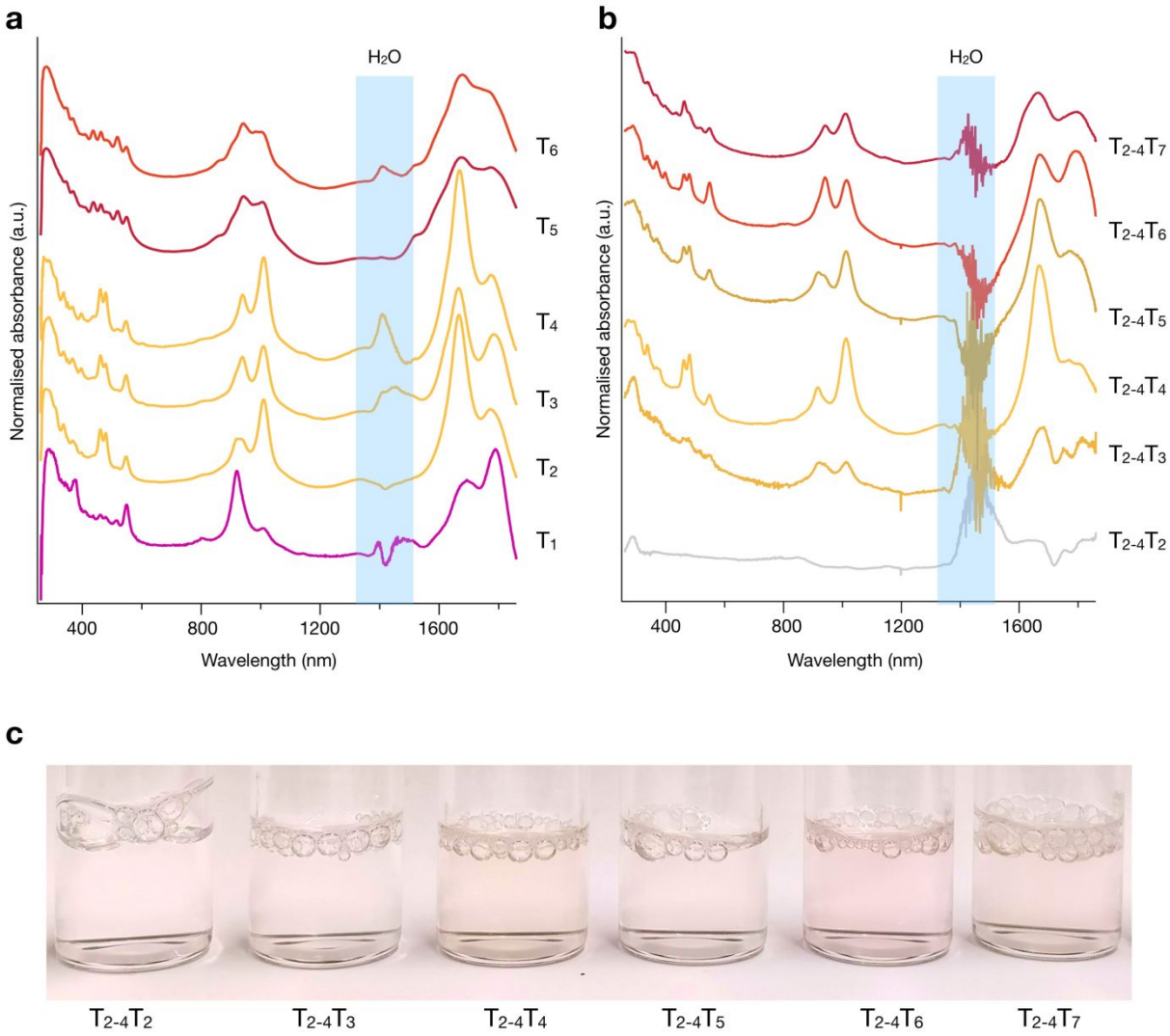

Supplementary Figure S9. Separation of the H_2O@EA2 semiconducting parent to demonstrate the robustness of our approach and investigate the importance of endohedral filling. (a) absorption spectra of Stage 1 fractions in H_2O ($T_1 - T_6$). $T_2 - T_4$ were found to be enriched in (14,6) and were combined to obtain $T_{2\text{-}4}$ and further processed at Stage 2 and the spectra are shown in (b). (c) a photograph provides the reader with an appreciation of the color and optical density of the resulting fractions. The spectra are normalised at 270 nm and offset vertically for better comparison.

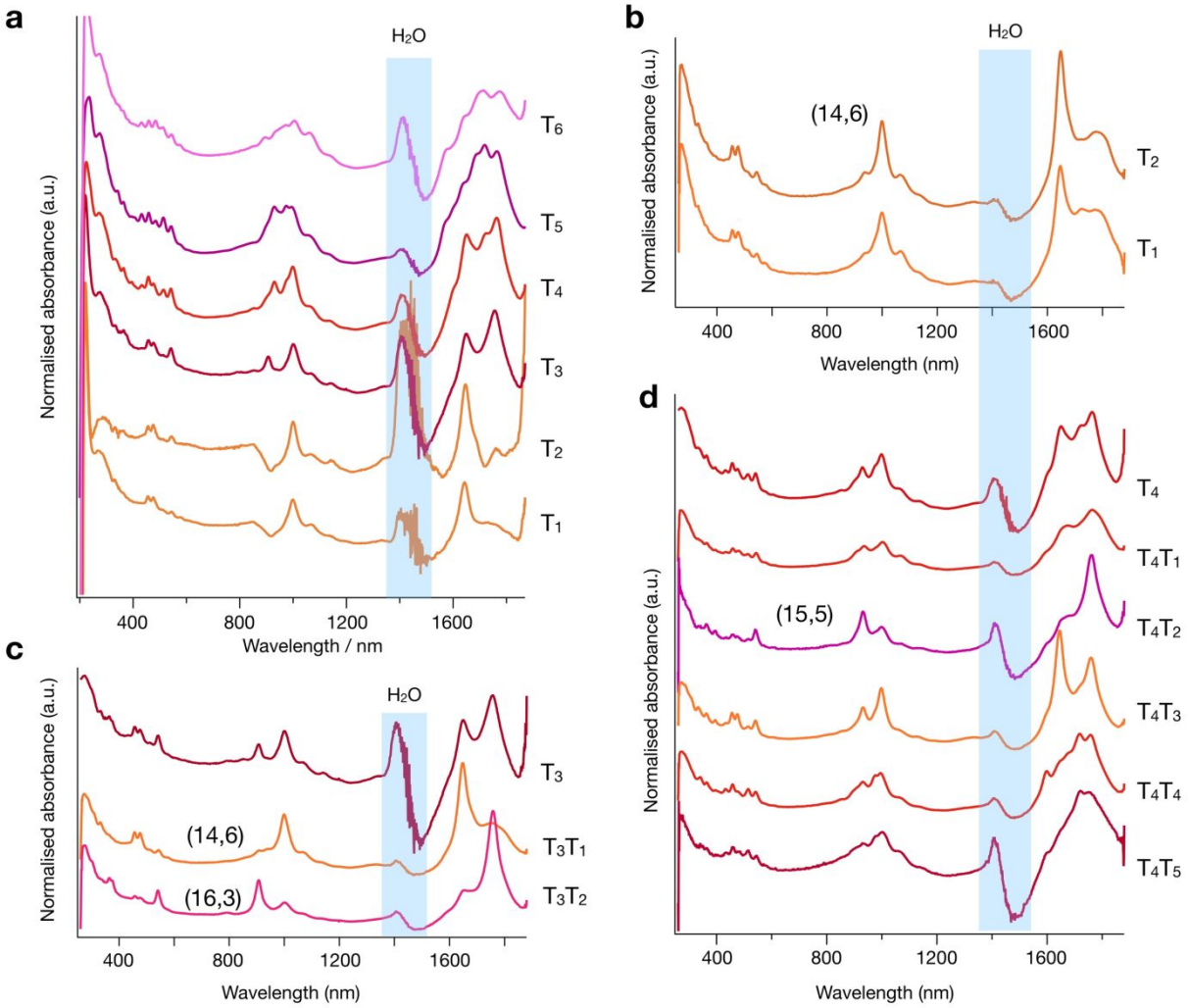

Supplementary Figure S10. Separation of the empty@EA-AP semiconducting parent to investigate the importance of endohedral filling. (a) absorption spectra of Stage 1 fractions in H_2O (T_1 – T_6). T_1 and T_2 were found to be enriched in (14,6) and were concentrated and their spectra are shown in (b). T_3 and T_4 were further processed at Stage 2 and their absorption spectra are shown in (c) and (d), respectively. More (14,6) and enriched (16,3) are found in T_3T_1 and T_3T_2, respectively, as well as (15,5) in T_4T_2. (e) a photograph provides the reader with an appreciation of the color and optical density of the resulting fractions. In all cases the top phase (T_n, PEG) was removed for measurement and replaced by fresh mimic top phase before adding further HCl. The spectra are normalised at 270 nm and offset vertically for better comparison.

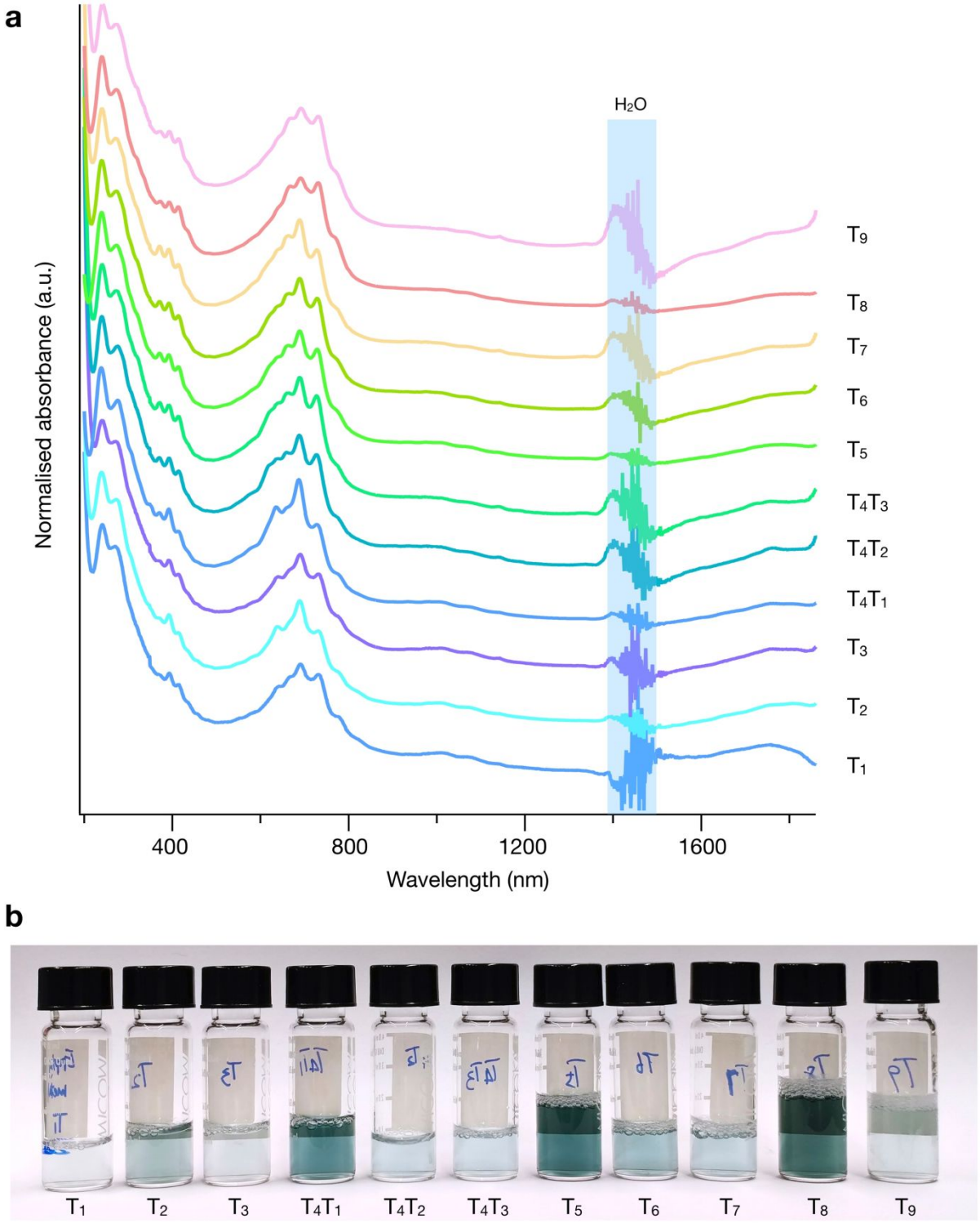

Supplementary Figure S11. Separation of the empty@EA-AP metallic parent to investigate the importance of endohedral filling. (a) absorption spectra of Stage 1 and Stage 2 fractions for T_4 in H_2O. (b) a photograph provides the reader with an appreciation of the color and optical density of the resulting fractions. The spectra are normalised at 270 nm and offset vertically for better comparison.

Circular Dichroism Measurements

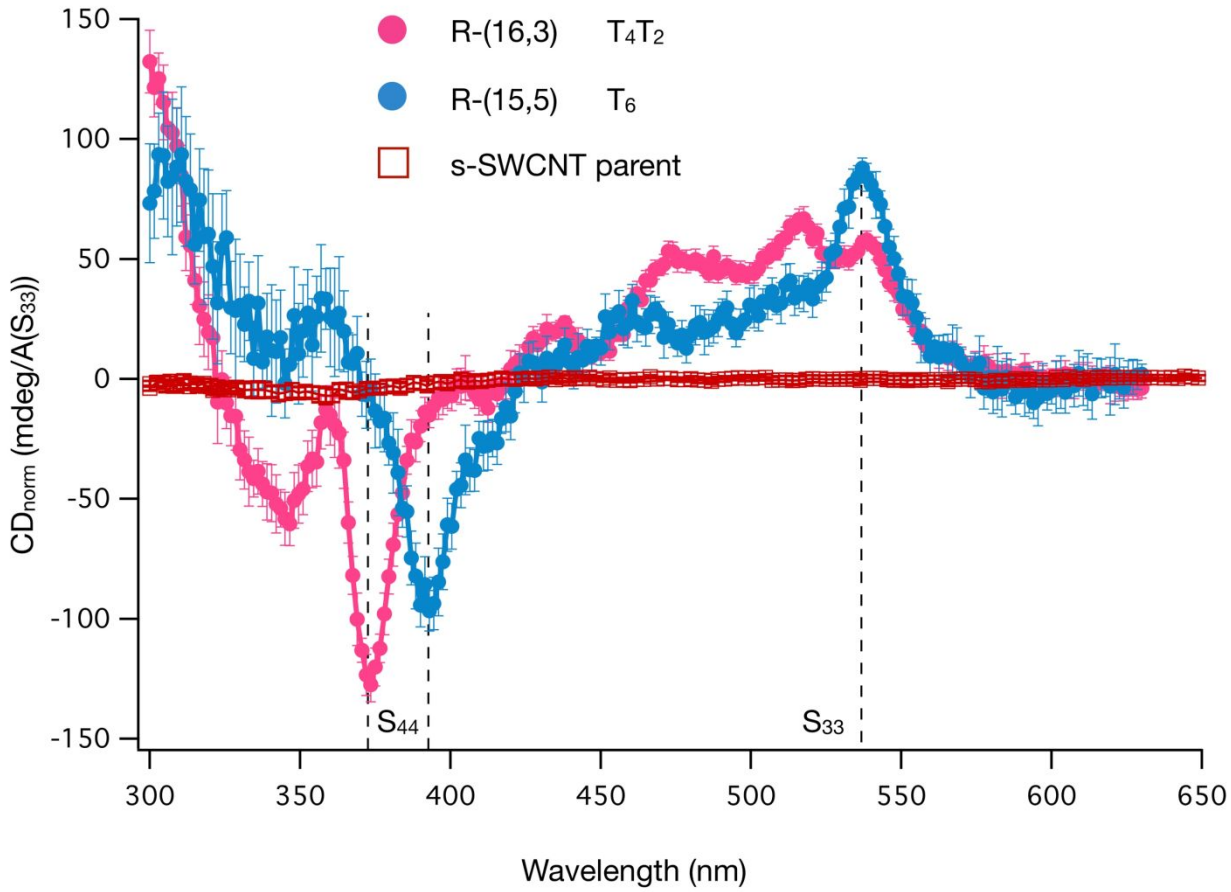

Supplementary Figure S12. Two fractions T_4T_2 and T_6 enriched in R-(16,3) and R-(15,5) from the $C_{16}H_{34}$@EA semiconducting parent. Circular dichroism spectra of isolated SWCNT fractions after subtraction of the reference spectrum and scaling by each individual fractions S_{33} absorption intensity. Each spectrum, including the reference spectrum (10.0 g/L DOC in D_2O), was measured 3 to 7 times, and the shown error bars represent k = 1 standard deviations of the propagated uncertainties. All samples were measured in the same 10.0 g/L DOC in D_2O solution environment used for the reference measurement.

PLE Data for Parent Dispersions and SWCNT (n,m) Fractions

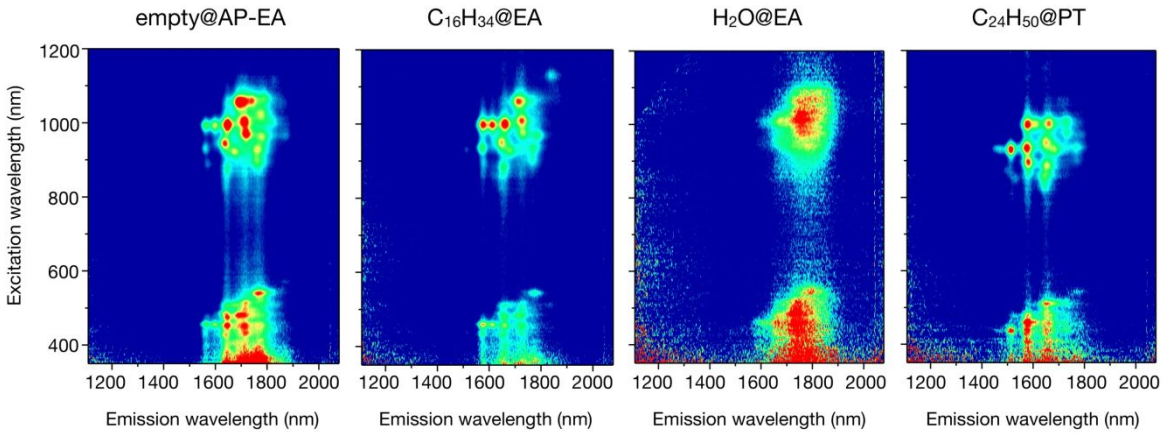

Supplementary Figure S13. 2D photoluminescence-excitation (PLE) maps of the different semiconducting parent suspensions used in this work. Note that the empty and alkane@SWCNT panel intensity scales are the same, whereas the H_2O@EA scale has been multiplied by a factor of 5 to enable visualization of the emission distribution. (Intensity was normalized over maximum absorption in the S_{11} range).

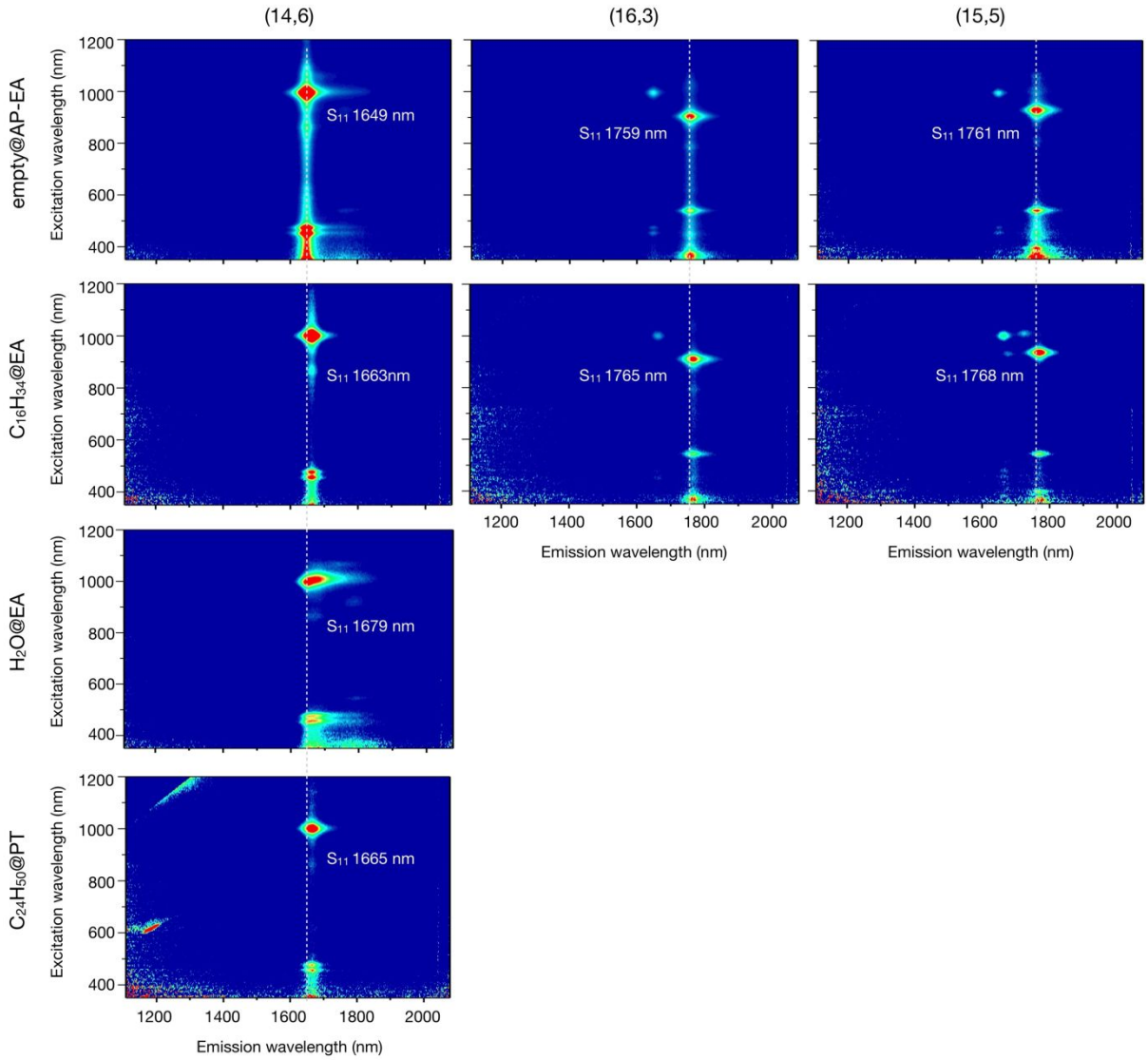

Supplementary Figure S14. 2D photoluminescence-excitation (PLE) maps of the different single chirality fractions prepared in this work with different endohedral fillings. A vertical dashed line indicates the position S_{11} for the empty carbon nanotube.

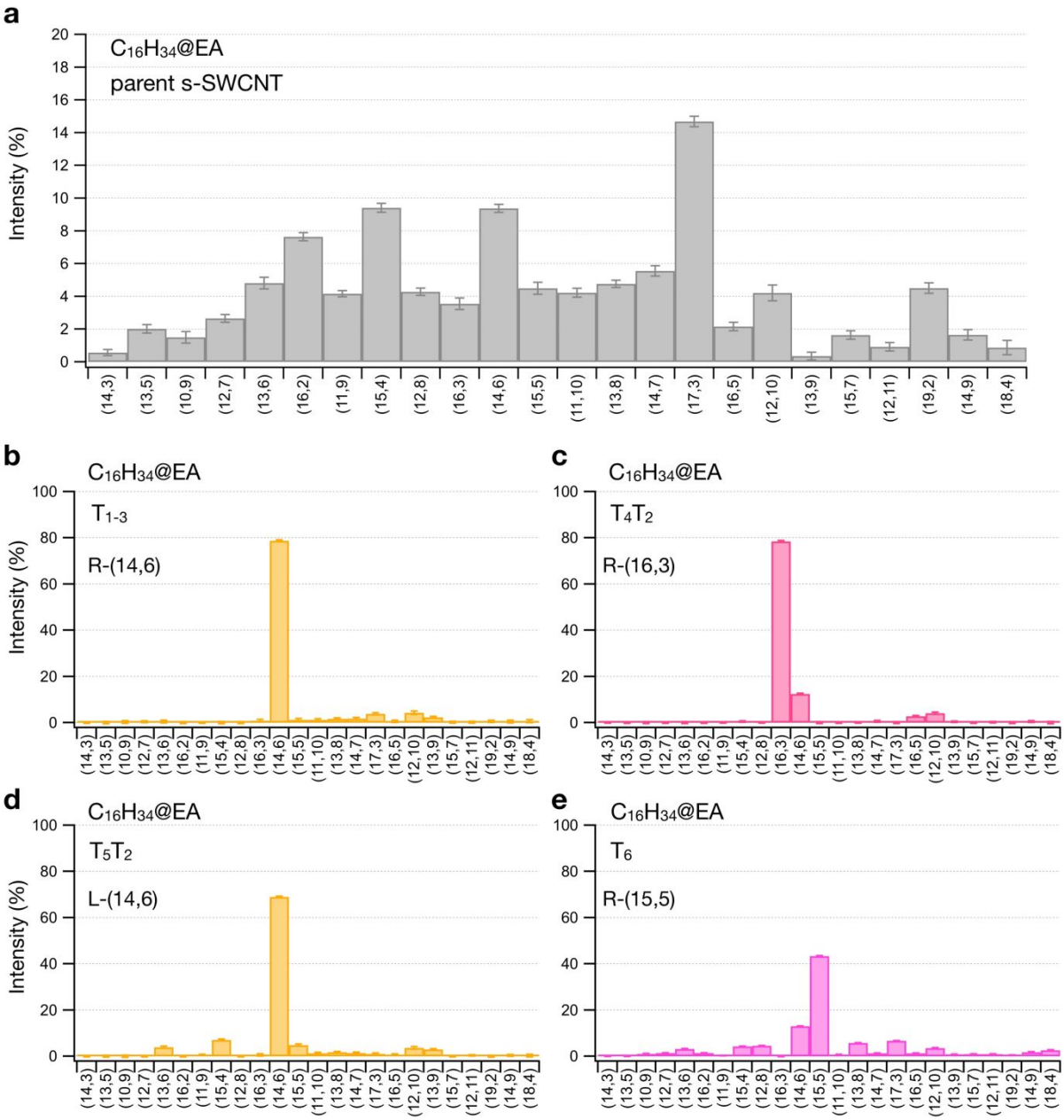

Supplementary Figure S15. Determination of (n,m) purity *via* histogram plots of the photoluminescence intensity of (a) the $C_{16}H_{34}$@EA semiconducting parent and the (n,m) purified fractions (b, c, d, e) obtained therefrom.

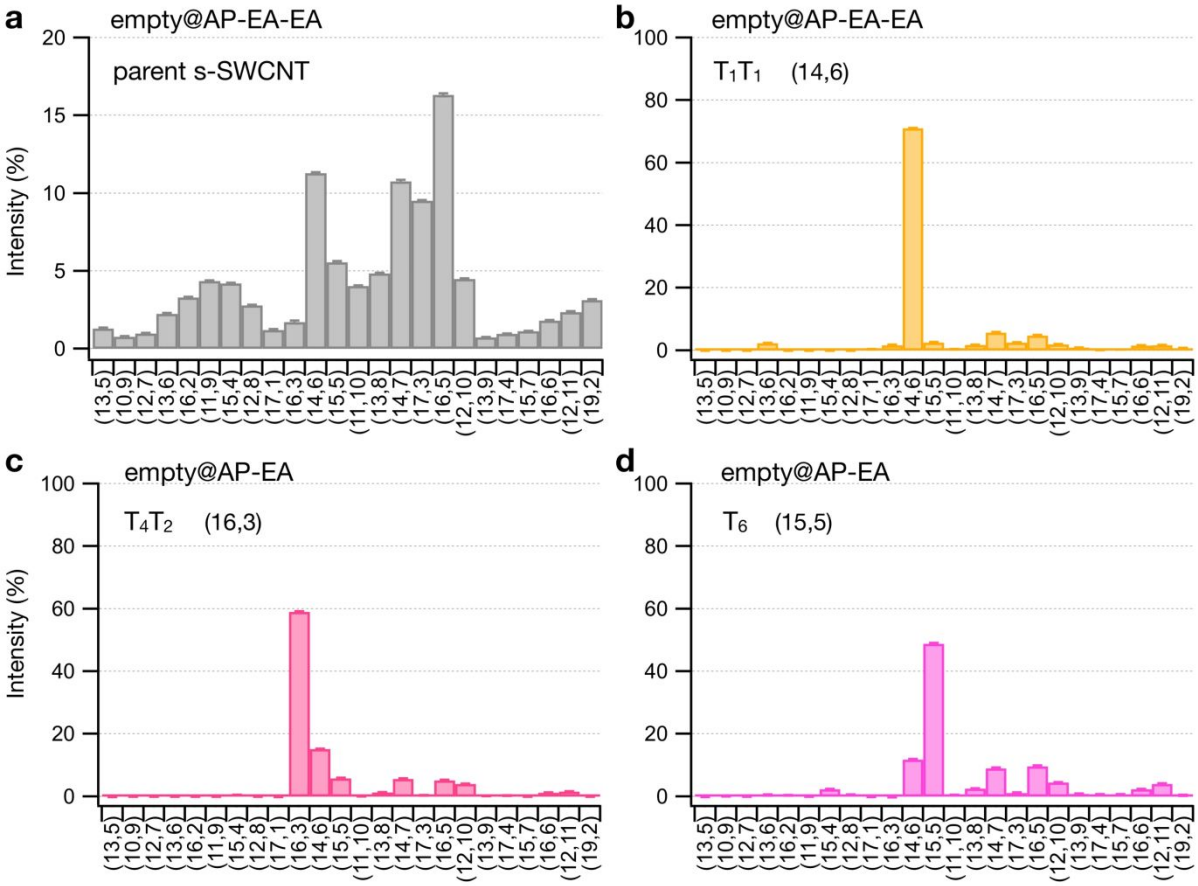

Supplementary Figure S16. Determination of (n,m) purity *via* histogram plots of the photoluminescence intensity of (a) the empty@EA-AP semiconducting parent and the (n,m) purified fractions (b, c, d) obtained therefrom.

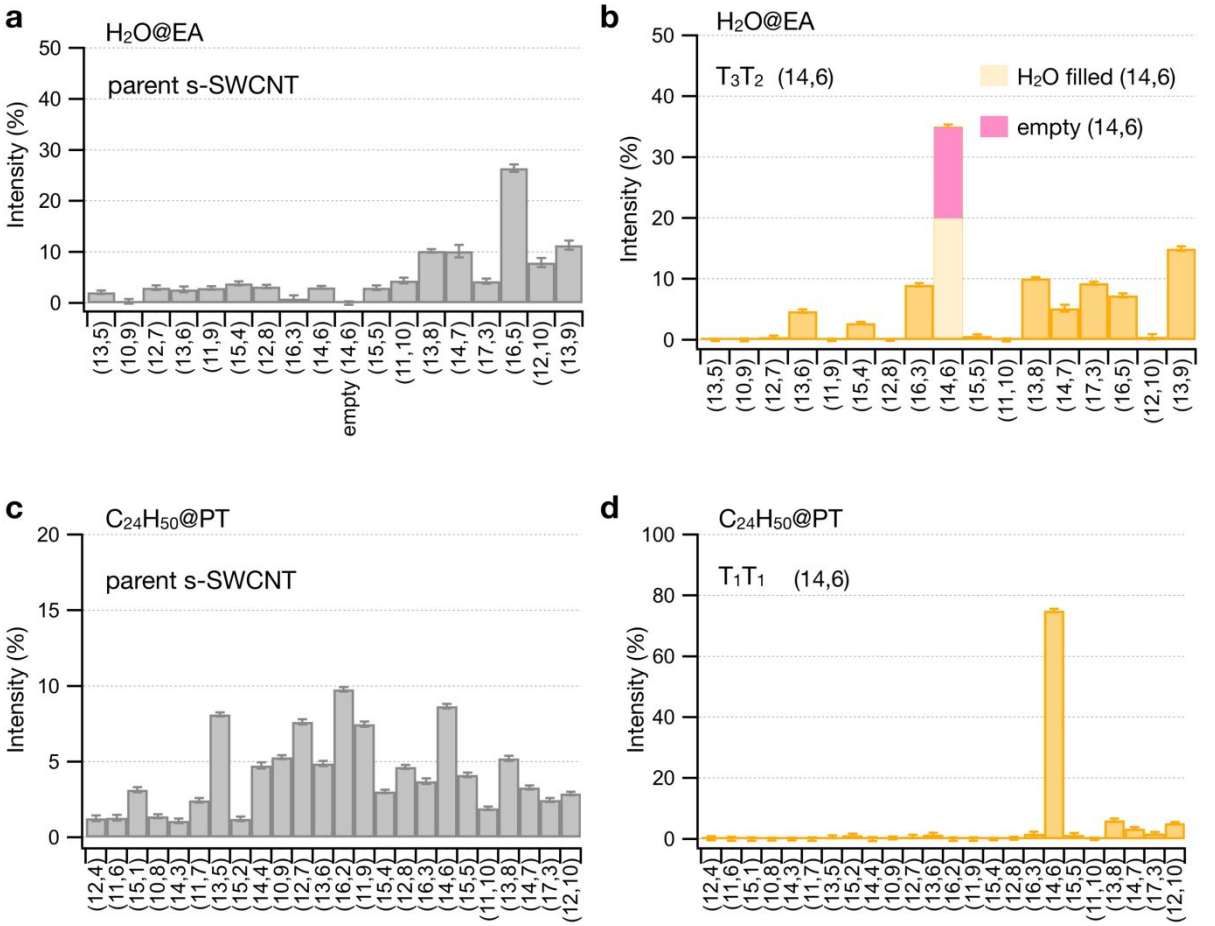

Supplementary Figure S17. Determination of (n,m) purity *via* histogram plots of the photoluminescence intensity of (a) the H_2O@EA semiconducting parent and (b) the (14,6) fractions obtained therefrom. (c) the $C_{24}H_{50}$@PT semiconducting parent and (d) the (14,6) fraction obtained therefrom.

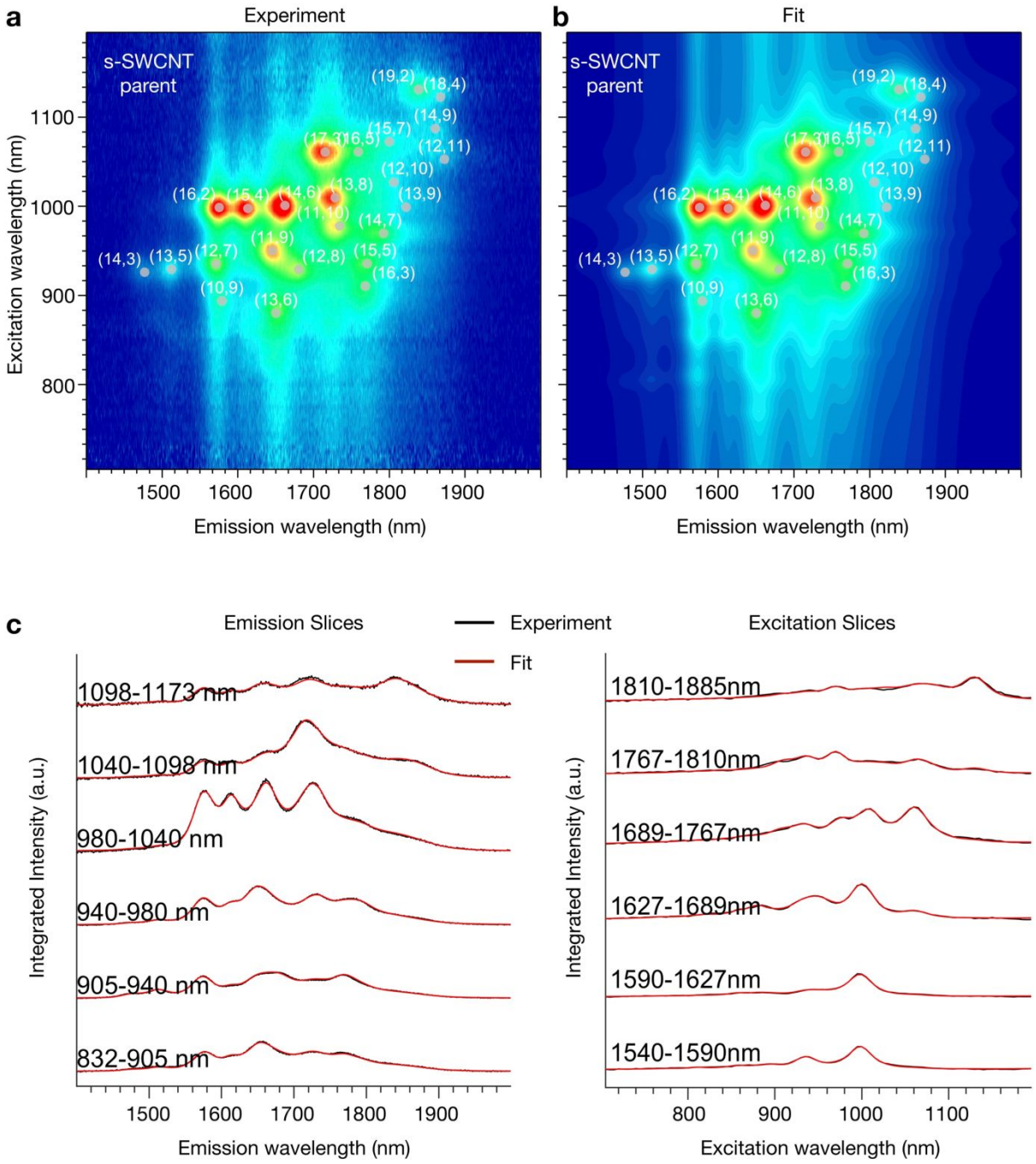

Supplementary Figure S18. Experimental (a) an fitted (b) PLE map of $C_{16}H_{34}$@EA semiconducting parent. (c) The emission and excitation slices show the quality of the fitting. Identified (n,m) speices are labeled.

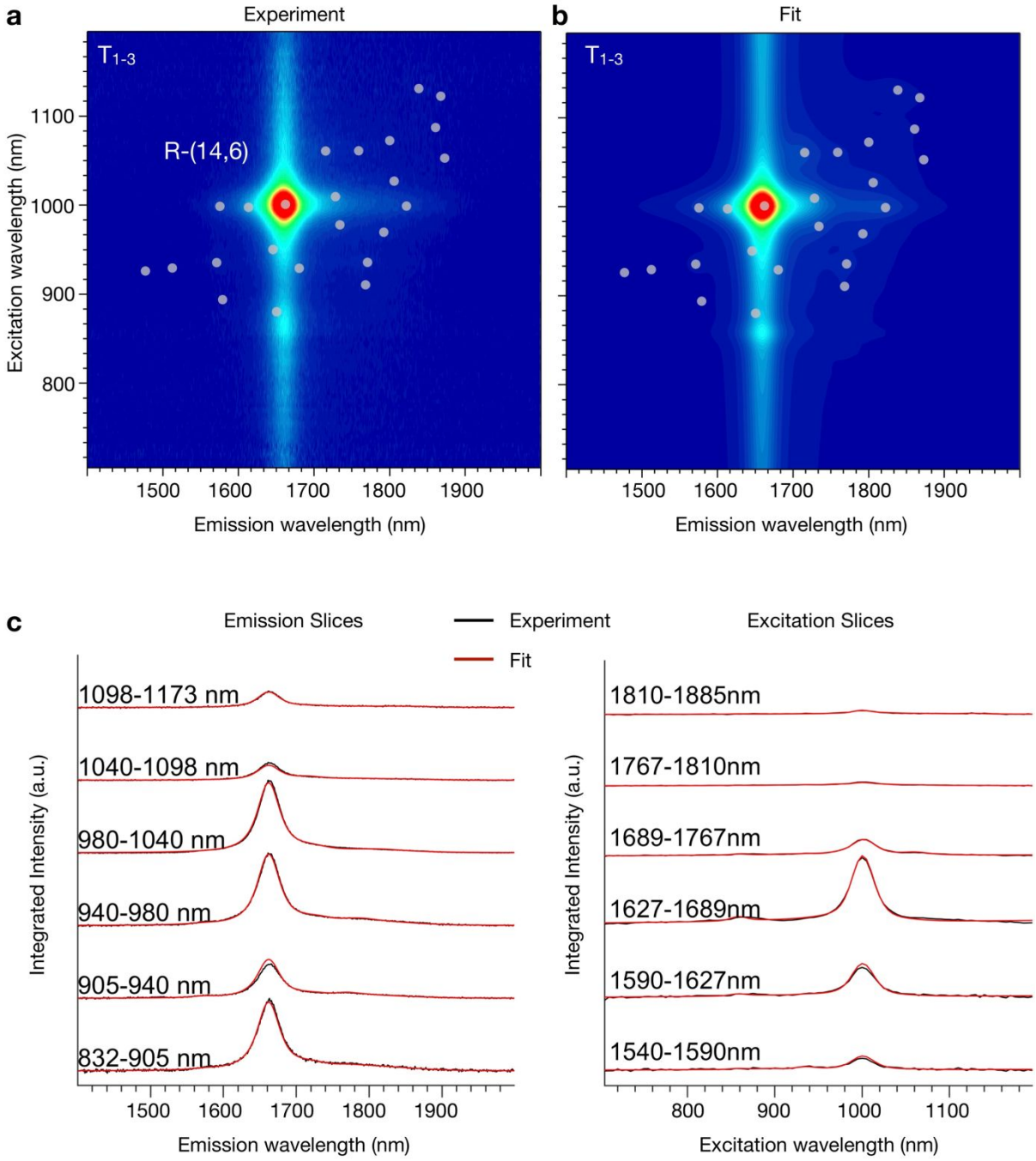

Supplementary Figure S19. Experimental (a) an fitted (b) PLE map of $T_{1\text{-}3}$ (R-(14,6)) separated from $C_{16}H_{34}$@EA semiconducting parent. (c) The emission and excitation slices show the quality of the fitting. Identified (n,m) speices are labeled. RBM phonon side bands in the emission spectrum and K-momentum dark exciton G-band phonon side bands in the excitation spectrum are clearly observed.

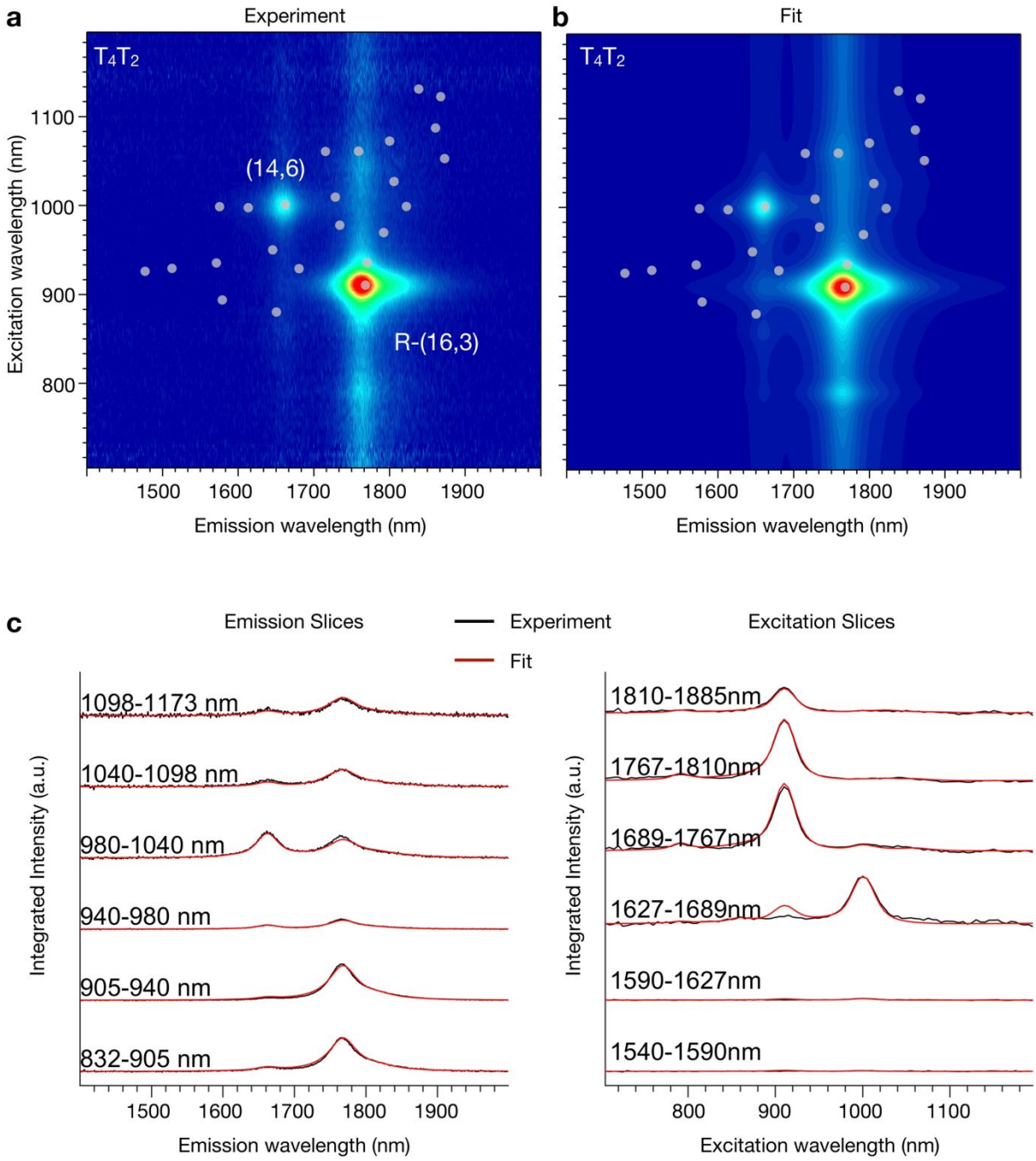

Supplementary Figure S20. Experimental (a) an fitted (b) PLE map of T_4T_2 (R-(16,3)) separated from $C_{16}H_{34}$@EA semiconducting parent. (c) The emission and excitation slices show the quality of the fitting. Identified (n,m) speices are labeled. RBM phonon side bands in the emission spectrum and K-momentum dark exciton G-band phonon side bands in the excitation spectrum are clearly observed.

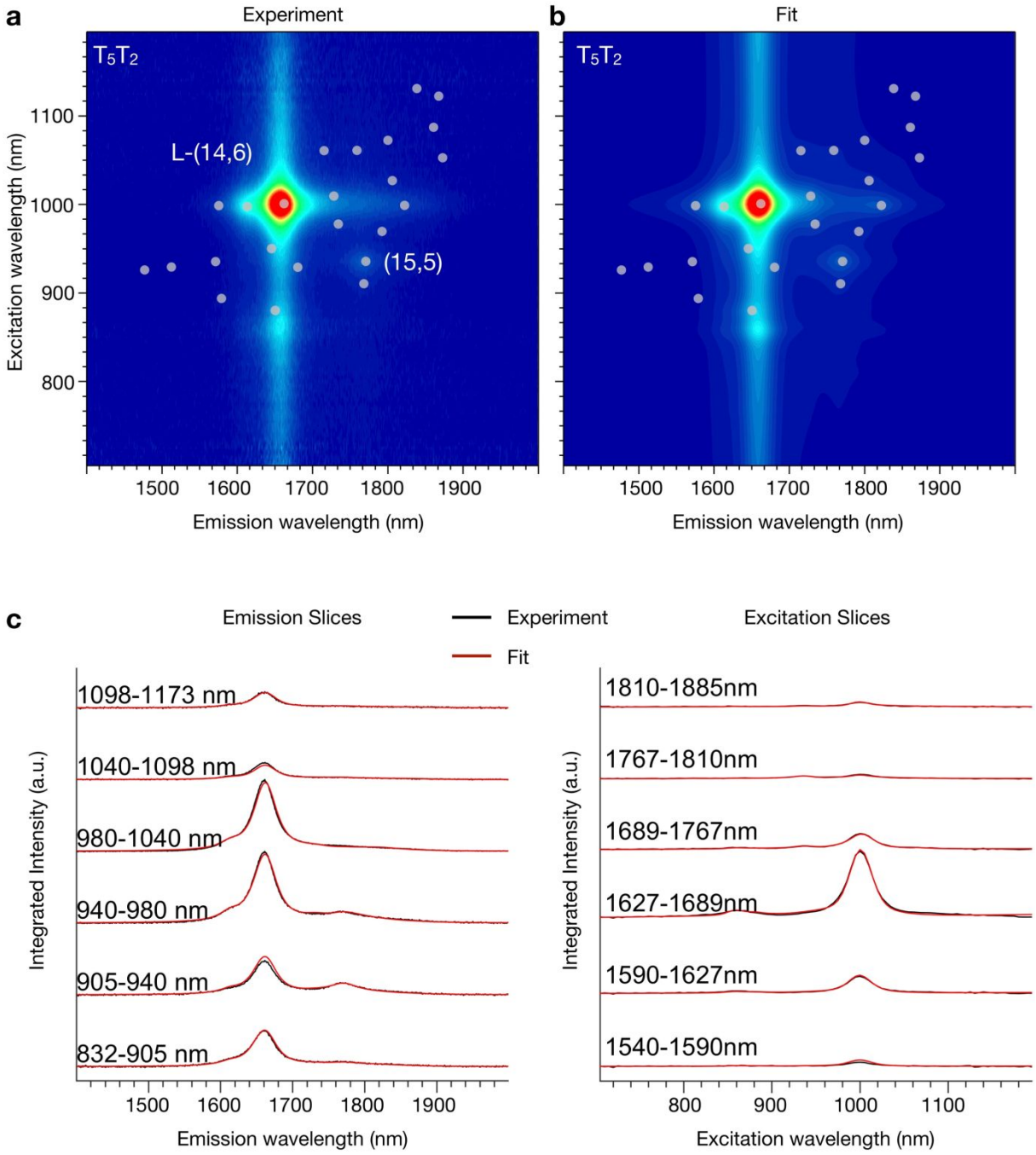

Supplementary Figure S21. Experimental (a) an fitted (b) PLE map of T_5T_2 (L-(14,6)) separated from $C_{16}H_{34}$@EA semiconducting parent. (c) The emission and excitation slices show the quality of the fitting. Identified (n,m) speices are labeled. RBM phonon side bands in the emission spectrum and K-momentum dark exciton G-band phonon side bands in the excitation spectrum are clearly observed.

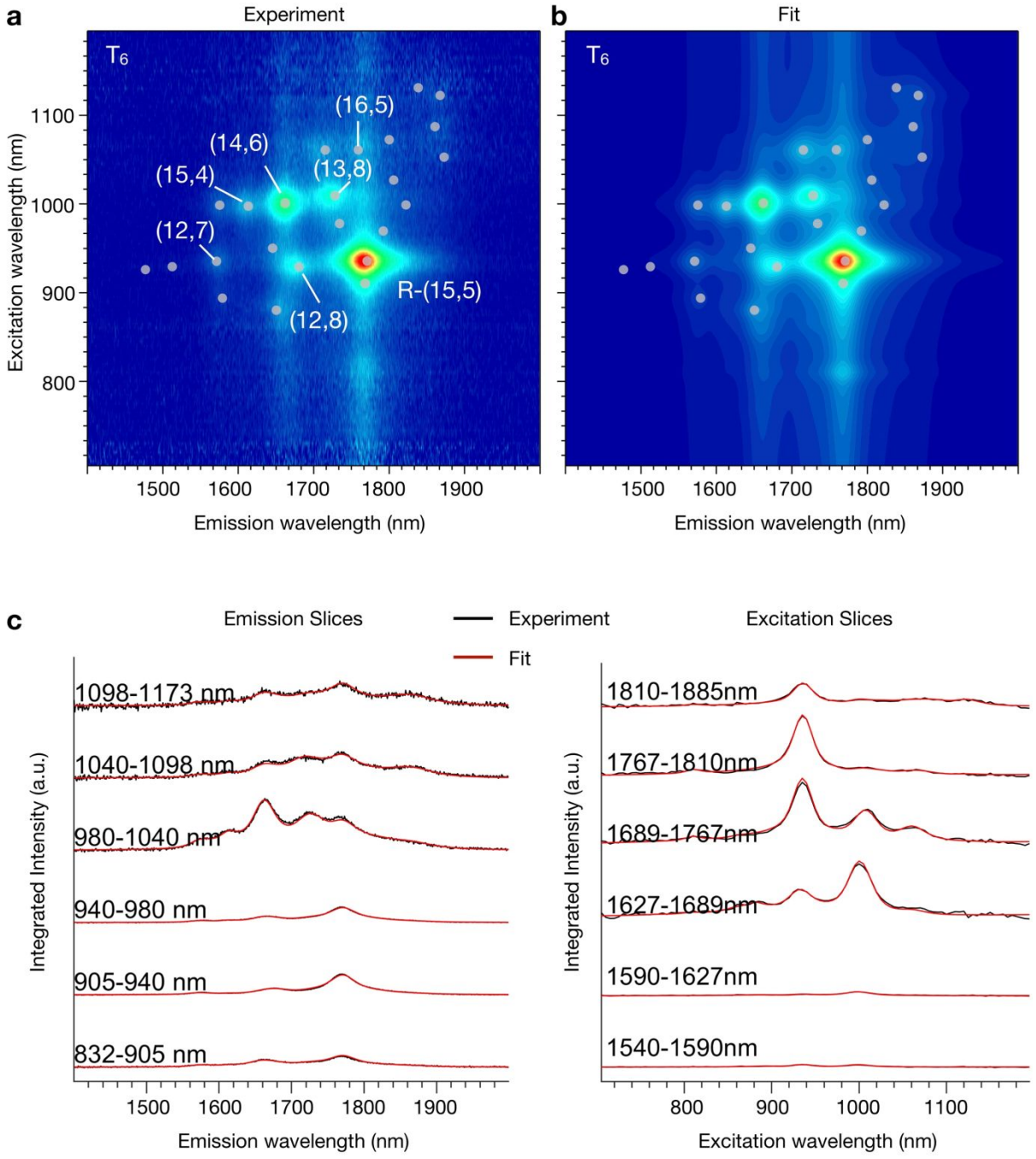

Supplementary Figure S22. Experimental (a) an fitted (b) PLE map of T_6 (R-(15,5)) separated from $C_{16}H_{34}$@EA semiconducting parent. (c) The emission and excitation slices show the quality of the fitting. Identified (n,m) speices are labeled. RBM phonon side bands in the emission spectrum and K-momentum dark exciton G-band phonon side bands in the excitation spectrum are clearly observed.

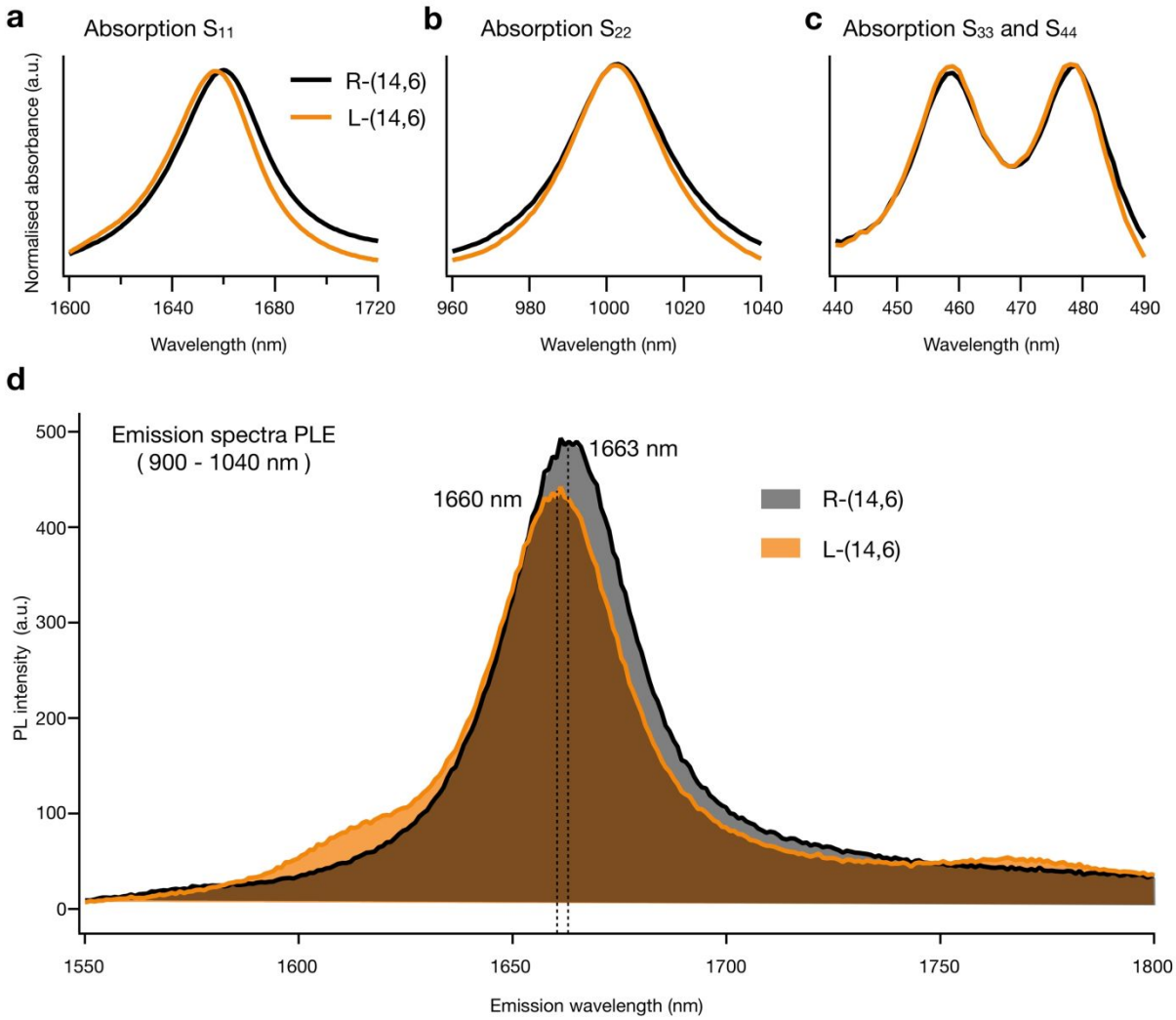

Supplementary Figure S23. (a) - (c) absorbance and (d) Photoluminescence spectra indicating the shift between the R-(14,6) ($T_{1\text{-}3}$) and L-(14,6) (T_5T_2) enantiomers from a $C_{16}H_{34}$@EA semiconducting separation.

Raman Scattering Data for Parent Dispersions and SWCNT (n,m) Fractions

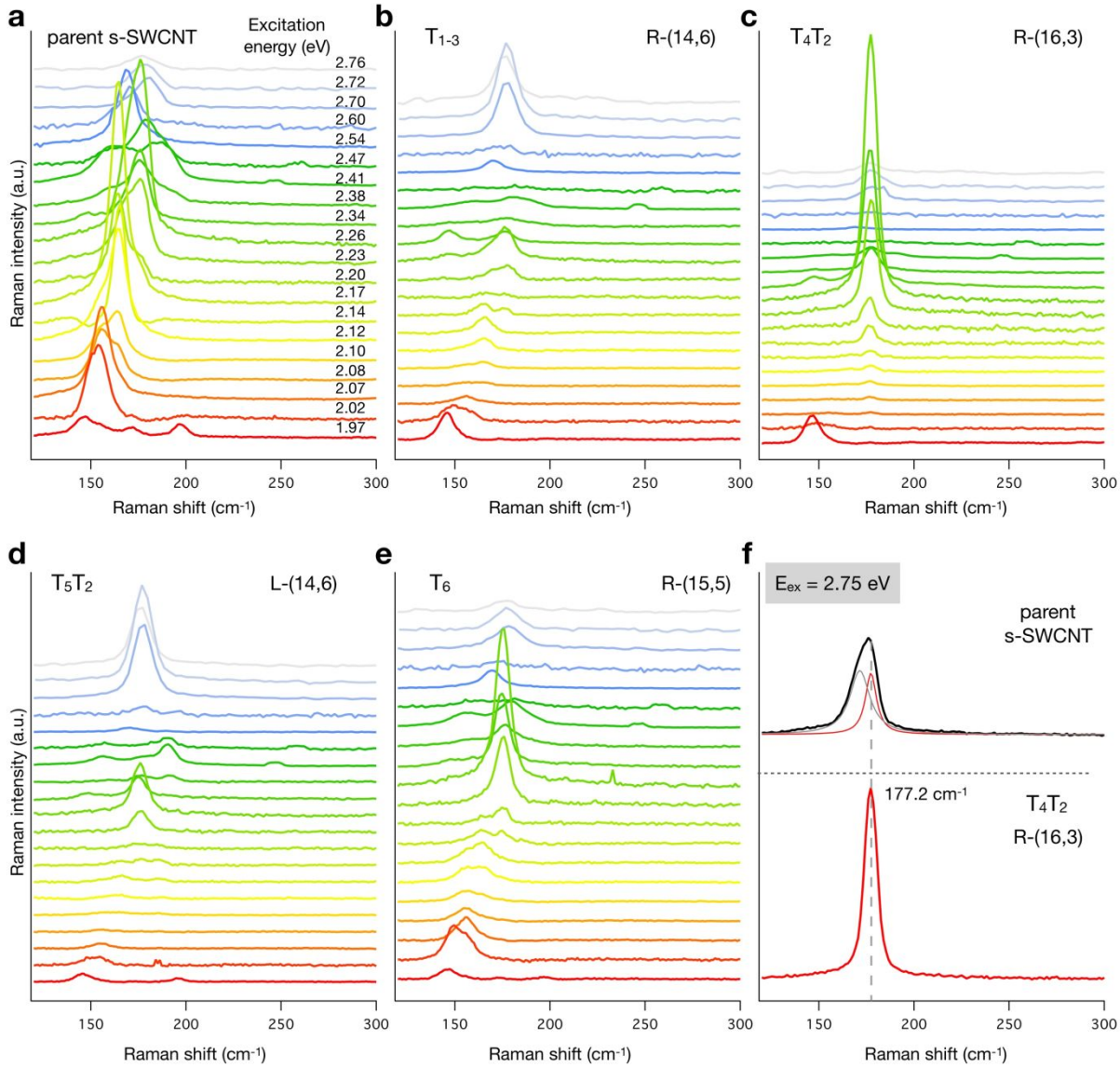

Supplementary Figure S24. Raman spectra measured at 20 different excitation energies. The radial breathing mode (RBM) spectra for the (a) semiconducting rich $C_{16}H_{34}$@EA parent suspensions along with those from purified fractions of (b) (14,6)-, (c) (16,3), (d) (14,6)+ and (e) (15,5) were used to generate the Raman maps shown in Figure 4. (f) comparison of the RBM spectra of the $C_{16}H_{34}$@EA parent semiconducting parent and (16, 3) with an excitation energy of 2.75 eV.

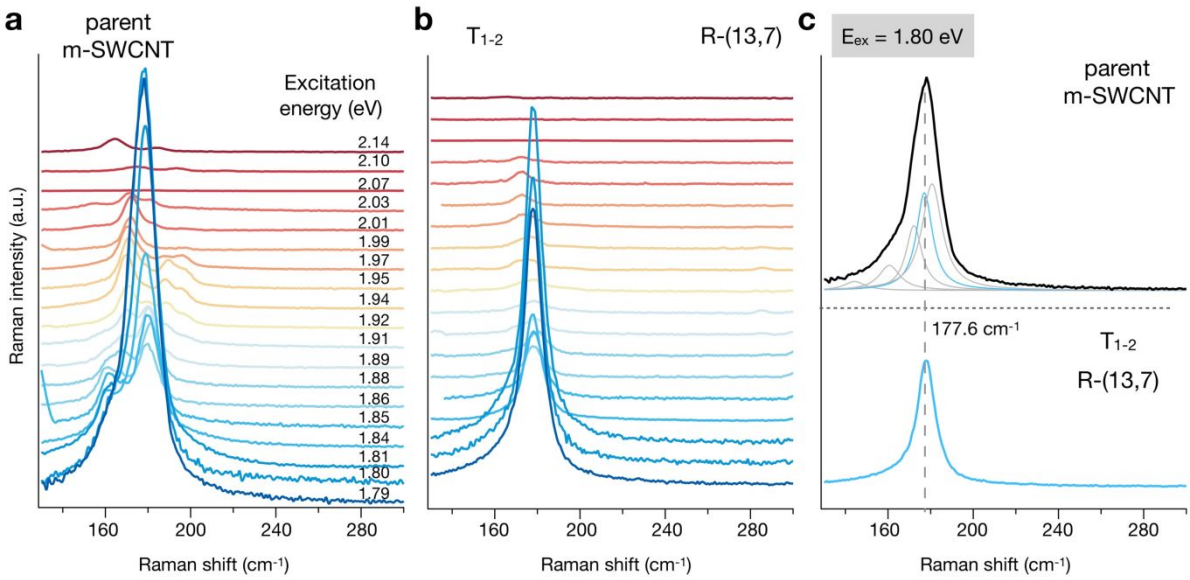

Supplementary Figure S25. Raman spectra measured at 19 different excitation energies. The radial breathing mode (RBM) spectra for the (a) metallic rich $C_{16}H_{34}$@EA parent suspensions and (b) (13,7) were used to generate the Raman maps shown in Figure 5. (c) comparison of the RBM spectra of the $C_{16}H_{34}$@EA parent metallic parent and (13, 7) with an excitation energy of 1.8 eV.

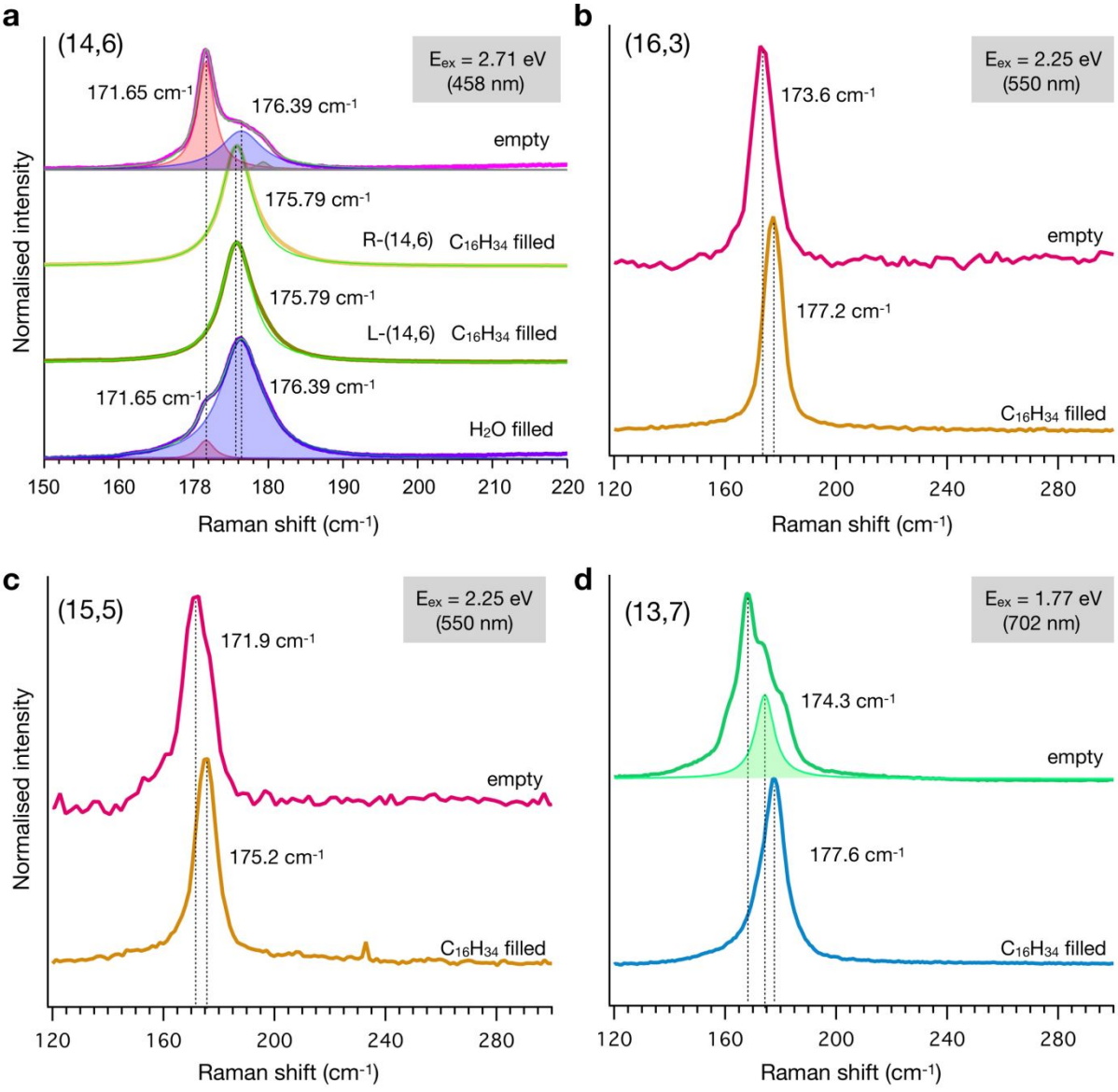

e

	(14,6)	(16,3)	(15,5)	(13,7)
calculated	173.8 cm^{-1}	174.6 cm^{-1}	171.7 cm^{-1}	175.6 cm^{-1}
empty	171.66 cm^{-1}	173.6 cm^{-1}	171.9 cm^{-1}	174.3 cm^{-1}
$C_{16}H_{34}$ filled	175.79 cm^{-1}	177.2 cm^{-1}	175.2 cm^{-1}	177.6 cm^{-1}
H_2O filled	176.39 cm^{-1}	-	-	-

Supplementary Figure S26. Radial breathing mode (RBM) Raman spectra indicating the Raman shift associated with empty or endohedrally filled ($C_{16}H_{34}$ or H_2O) fractions of (a) (14,6), (b) (16,3), (c) (15,5) and (d) (13,7). Each SWCNT species was excited at its resonance energy and is indicated in the figure. (e) tabulated Raman shift associated with the different endohedral fillings.

(n,m)	E_{ii}	RBM_{alkane}, cm^{-1}	RBM_{empty}, cm^{-1}	E_{ii}^{alkane}, eV	E_{ii}^{empty}, eV	ΔE, meV
(14,6)	S_{44}	177.3	172.4	2.71	2.75	-40
(15,5)	S_{33}	175.2	170.2	2.28	2.29	-10
(16,3)	S_{33}	177.2	173.1	2.28	2.29	-10
(13,7)	M_{11}^{L}	177.6	174.1	1.80	1.83	-30

Supplementary Table S8. Optical properties of the enriched large-diameter nanotubes. Type of transition, RBM frequencies of the alkane-filled nanotubes from this work compare to empty nanotubes from Refs.[4, 5], $\Delta E = E_{ii}^{empty} - E_{ii}^{alkane}$

Device Data for Additional Field Effect Transistor Devices

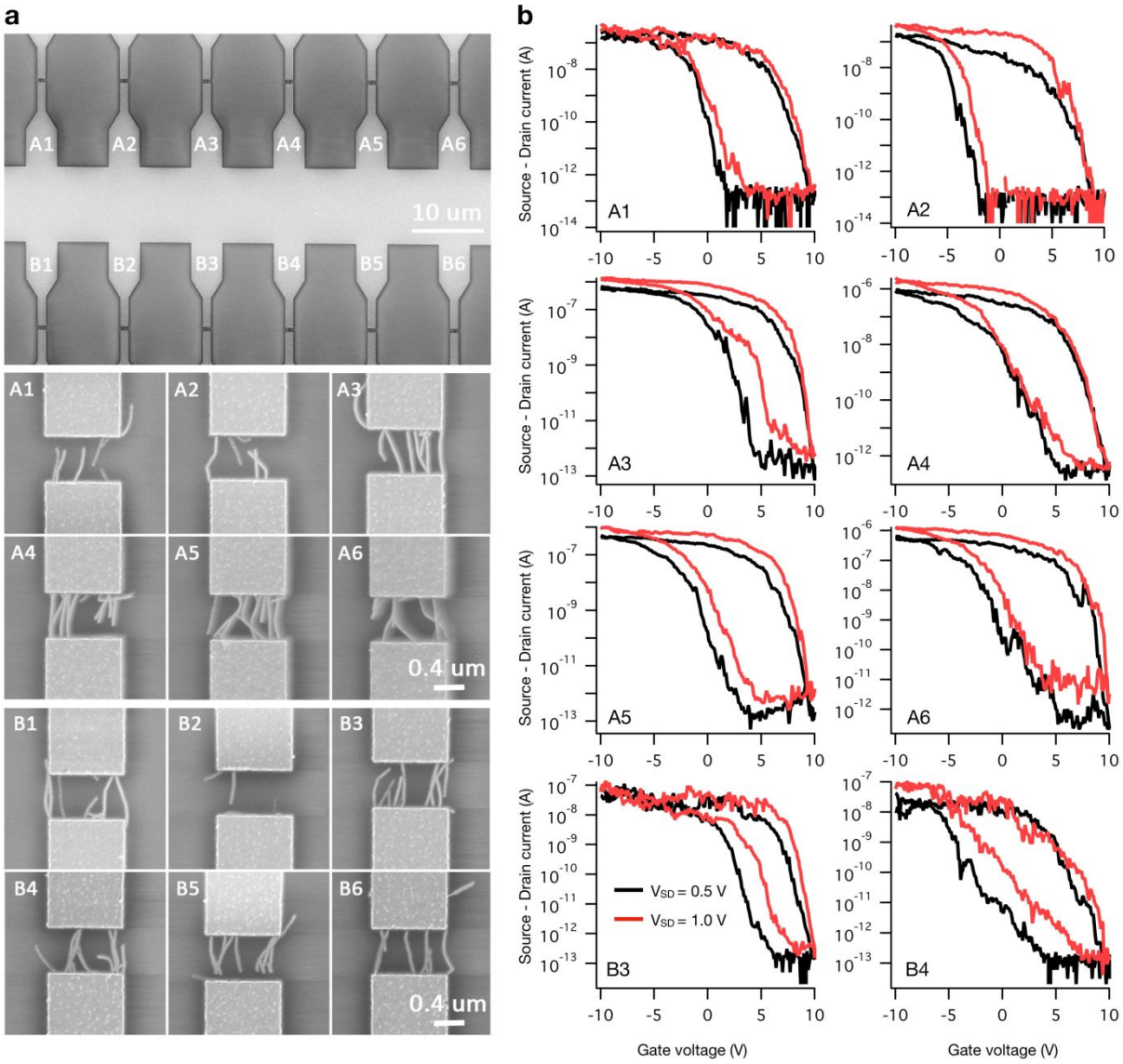

Supplementary Figure S27. (a) SEM images of 12 CNT-FETs (A1 – A6 and B1 – B6) prepared from $C_{16}H_{34}$@(14,6) and (b) corresponding transconductance measurements with an applied source drain voltage (V_{SD}) of 0.5 V (black) and 1.0 V (red).

References

1. Cambré, S.; Campo, J.; Beirnaert, C.; Verlackt, C.; Cool, P.; Wenseleers, W., Asymmetric Dyes Align Inside Carbon Nanotubes to Yield a Large Nonlinear Optical Response. *Nat. Nanotechnol.* **2015,** *10*, 248-252.
2. Bachilo, S. M.; Strano, M. S.; Kittrell, C.; Hauge, R. H.; Smalley, R. E.; Weisman, R. B., Structure-Assigned Optical Spectra of Single-Walled Carbon Nanotubes. *Science* **2002,** *298*, 2361-2366.
3. Cambre, S.; Wenseleers, W., Separation and Diameter-Sorting of Empty (End-Capped) and Water-Filled (Open) Carbon Nanotubes by Density Gradient Ultracentrifugation. *Angew. Chem. Int. Edit.* **2011,** *50*, 2764-2768.
4. Araujo, P. T.; Jorio, A.; Dresselhaus, M. S.; Sato, K.; Saito, R., Diameter Dependence of the Dielectric Constant for the Excitonic Transition Energy of Single-Wall Carbon Nanotubes. *Phys. Rev. Lett.* **2009,** *103*, 146802.
5. Doorn, S. K.; Araujo, P. T.; Hata, K.; Jorio, A., Excitons and Exciton-Phonon Coupling in Metallic Single-Walled Carbon Nanotubes: Resonance Raman Spectroscopy. *Phys. Rev. B* **2008,** *78*, 165408.